NOVEMBER 1984   LRP 241/84

TARGET PLASMA CONDITIONS IN TCA

A. de Chambrier, G.A. Collins, Ch. Hollenstein,

B. Joye, J.B. Lister, J.-M. Moret, S. Nowak,

A. Pochelon, W. Simm

TARGET PLASMA CONDITIONS IN TCA

A. de Chambrier, G.A. Collins, Ch. Hollenstein, B. Joye,
J.B. Lister, J.-M. Moret, S. Nowak*, A. Pochelon, W. Simm

Centre de Recherches en Physique des Plasmas
Association Euratom – Confédération Suisse
Ecole Polytechnique Fédérale de Lausanne
21, av. des Bains - 1007 Lausanne / Switzerland

*University of Fribourg, Switzerland

ABSTRACT

We discuss the conditions of the target plasma in the TCA tokamak prior to the rf heating pulse. The toroidal field and plasma current are held fixed and the density is varied from $\bar{n}_e \sim 0.5 \times 10^{13}$ to 5×10^{13} cm^{-3}. Both hydrogen and deuterium discharges are considered. The density and gas dependence of the macroscopic plasma parameters is analysed, as well as the impurity and energy content. We observe an increasing peaking of the electron density profile as the density is increased. This observation is compatible with other small tokamaks and we present a density profile scaling law that depends on the Murakami parameter $n_e(0)R_0/B_\phi$. We find that for this range of density, the global energy confinement time is proportional to the line density as is typically the case before the saturation of "Alcator Scaling" which provides an adequate representation of the data. We perform a radial electron power balance in order to estimate the electron thermal conductivity $n_e\chi_e$. Its value at half radius is around 4×10^{17} cm^{-1}s^{-1} for the lowest density discharges and decreasing to 2×10^{17} cm^{-1}s^{-1} at the highest density. The diagnostics used for this study are also briefly described, together with their analysis techniques.

I. INTRODUCTION

The TCA tokamak has been described in detail [1] and has the following characteristics :

$$B_\emptyset \leqslant 15.2 \text{ kG}$$
$$I_p \leqslant 170 \text{ kA}$$
$$R_0, a = 61.5, 18.0 \text{ cm}$$
$$n_e(0) \leqslant 10^{14} \text{ cm}^{-3}$$
$$t_{pl} \sim 100 \text{ msec flat-top.}$$

The experiment is mainly dedicated to the study of Alfvén Wave Heating. The first experiments carried out showed heating but also an increased impurity content [2]. Changes in limiters and antenna design have led to considerable improvement [3]. Standard discharges, made with bare carbon limiters and TiN coated bar antennae without screens, have $P_{rad}(0)/P_{oh}(0) \sim 5\%$ and TCA can now be considered to produce a clean target plasma. We therefore have systematically studied the ohmically heated target plasmas used for the rf experiments. Typically in these rf experiments we vary the target plasma density over a wide range, as well as the working gas, mainly due to the fact that both change the Alfvén Wave resonance structure.

In this report we discuss the conditions in which the measurements were carried out (section II), the diagnostics used and their analysis (section III) and the results from the density scans in both hydrogen and deuterium as the working gas (section IV).

II. EXPERIMENTAL CONDITIONS

a) Torus

The torus is stainless steel (316 LN), of rectangular cross-section, with a minimum limiter radius to wall separation of 35 mm at the inside wall (Fig. 1). The pumping speed at the torus is ~300 l/sec. The vessel is prepared for tokamak operation as follows. After opening to air, and after pumping to ~2x10^{-7} Torr(G), the Viton O-rings are heated to ~90 °C, using the cooling circuit, for several hours. A

continuous a.f. discharge (5 kHz) is then run in Argon at $\sim 2 \times 10^{-4}$ Torr(G) for one hour, during which the torus heats up to 80 °C. This is then normally repeated the following day. The mass spectrum of the background gas is then as shown in Fig. 2a). Regular Taylor Cleaning (2x30 ms a.f. pulses/sec) is then carried out each night for ~ 10 hours in the working gas to be used during the following day. Typical mass-spectra of the prepared torus are shown in Fig. 2b) for H_2 and 2c) for D_2 operation. The base pressure is typically 2.0×10^{-7} Torr(G) after the cleaning due to outgassing of the loaded walls, and it drops to typically 8×10^{-8} Torr(G) after prolonged pumping over a weekend. The mass-spectrum of the residual gas after a normal tokamak shot is shown in Fig. 2d) for H_2 operation and Fig. 2e) for D_2 operation, in which we see a large production of hydrocarbons from the uncoated carbon limiters. The pump-down curves for some residual gas masses after a tokamak shot are shown in Fig. 3.

b) Plasma Operation

The target plasma for this work was run at 133 kA under active current-feedback control for a pulse-length of ~ 120 msec at which time the loop voltage is cut. The toroidal field was set to 15.2 kG, giving $q(a) \sim 3$. A typical discharge is shown in Fig. 4, of which only the period before the rf pulse is used for this study. A total of 0.49 Volt-seconds is consumed before the primary current reaches zero. The plasma current is ramped up at $\sim 4-7$ kA/msec to its preset value. The working gas is injected 15-20 msec before the breakdown and the piezo-electric valve is operated under feedback control to maintain a pre-determined density waveform. During regular operation a 5-minute shot cycle is operated, limited by the toroidal field coil cooling.

III. DIAGNOSTICS AND THEIR ANALYSIS

The following diagnostics were used regularly on TCA during these scans :
- EM diagnostics
- Visible spectroscopy
- Interferometers: 2 mm, 0.5 mm

- X-rays: T_e by filters, Pinhole camera, Hard-X
- Bolometer: single chord scannable
- Thomson Scattering: one-pulse, one-point
- E.C.E.: scanning Michelson interferometer
- Neutral Particle Analyser: 5 channels, one-chord
- Langmuir probes.

The layout of these diagnostics is shown in Fig. 5 and they will now be discussed in turn.

a) <u>EM diagnostics</u>

The loop-voltage is measured by a single-turn shielded loop at R ~40.5 cm, Z ~26 cm in a region where there is little stray field from the OH-coil. We have also compared its signals with the total gap-voltages. The $L_p\dot{I}_p$ correction is made using a value of L_p chosen to remove the discontinuity in $V_R=V_L-L_p\dot{I}_p$ when a voltage step is applied to the OH-coil.

The plasma current is measured using a single-turn Rogowski coil wound outside the torus.

The horizontal position of the centre-of-gravity of the current distribution is measured using a modified "cos-coil" wound on a square cradle outside the torus. Its winding density was numerically calculated not only to take into account the square frame but also a) to remove the offset due to toroidicity and b) to linearize the response as a function of displacement of the current centre-of-gravity (c.g.). The response was tested using a toroidal loop of variable radius. The vertical position of the current c.g. is similarly measured using a numerically calculated "sine-coil". Both coils are sensitive to net poloidal fields and these effects are subtracted electronically in the screened room. In the horizontal position feedback loop, allowance is made for the distance between the current c.g. and the outer surface centre. For typical profiles, the current c.g. is roughly at 1/3 of the distance from the magnetic axis to the outer surface centre.

The paramagnetical increase in toroidal flux is measured using a

multi-turn "diamagnetic" loop. Absolute calibration of this loop has not yet proved possible and an improved loop has been constructed. We calculate simply

$$\beta_\perp = 1 - \frac{8\pi B_\phi \Delta\phi}{\mu_0^2 I_p^2}$$

noting that this value is almost independent of both plasma position and shape.

The high frequency modulation of the plasma poloidal field at ~5-20 kHz is measured by pick-up loops in a ceramic tube placed in the shadow of the limiters. This measurement is used for plasma set-up to avoid spending too much time in regions close to integral values of the safety factor q during the current build-up.

In addition the various poloidal control winding currents are measured using standard Rogowskis.

b) Spectroscopic Measurements

We observe the $H_\alpha + D_\alpha$ emission ($\lambda \cong 6563$ Å) through a narrow band interference filter ($\lambda_0 = 6563 \pm 5$ Å) using a standard photomultiplier tube (EMI 9658 B). The light is collimated to ±3.6 mrad, much narrower than the equivalent filter-bandwidth. One diameter is viewed, well away from the limiters, as a fixed measurement. A second $H_\alpha + D_\alpha$ monitor is used to observe toroidal asymmetries in the emission, viewing through all available ports.

In addition we observe the emission of OII (4415 Å) and FeII (2599 Å), again using PM+interference-filter combinations, with filter transmissions given by 4415±10 Å and 2600±120 Å respectively.

Specially designed dynode chains are used for all tubes, giving a linear response for pulses up to 5 mA x 1 kΩ x 5 msec. This avoids saturation during the initial ionization pulse.

c) Interferometry

A 140 GHz interferometer is used with a 5 mW Gunn diode source as

a regular monitor of line-averaged plasma density, and has already been described [4]. The published technique using a circulator for switching in a $\pi/2$ phase-shift was replaced in 1982 by modulation of the diode source voltage with a simple square-wave. Since the source output frequency is slightly voltage dependent, we arrange that the product path-length x $\Delta f/c$ is equal to 1/4. In this way we have been able to dispense with the lossy circulator element. The new system also requires much less setting up effort. Its total phase analogue output is also used for feedback control of the plasma density.

Electron density profile measurements are performed with an 8 channel FIR interferometer ($y=R-R_0=-15.5$, -10.5, -6.5, -2.5, 1.5, 5.5, 10.5, 15.5 cm). It uses a 10 mW CH_3I laser ($\lambda=447$ μm) optically pumped by a CO_2 laser. The optical set-up is similar to that used on TFR [5]: the reference beam and the 8 plasma beams are mixed with a frequency shifted beam (5-20 kHz, depending on the time resolution required), producing low frequency beating. The phase shift is then measured with an electronic clock timing the interval between zero-crossings of the reference and the plasma signals. Fringe jumps are interpreted by the time derivative of the phase. Fig. 6 shows the typical behaviour of the line-integrated densities.

Some studies are made without inverting the profiles, but when necessary, an asymmetric Abel inversion is used [6]. First a polynomial or a cubic spline is fitted to the discrete data to give a continuous phase shift $\Phi(y)$ ($y=R-R_0$); the density is then calculated as $n(r,y)=n_0(r)(1+u(y))$, where n_0 is found by applying Barr's inversion [7] to the even part of Φ and u is the odd part of Φ (Fig. 7). The central density is not sensitive to the fitting used, although a polynomial of too high an order produces artificial oscillations. The profiles are also stable to imposing a zero phase shift at a position further out than the limiter radius. Imposing a smaller plasma radius causes problems for the inversion (Fig. 8).

d) X-rays

The electron temperature of the plasma is determined by using soft X-ray diagnostics. The so-called "two-foil absorber" method [8],

relies on the a priori assumption that the X-ray power spectrum of a Maxwellian plasma varies as $\exp(-E/T_e)$ [9] and the fact that the transmission coefficient of X-rays through thin foils is strongly energy dependent. Thus T_e can be calculated to a good approximation using a formula of the type :

$$T_e [eV] = \frac{a [eV]}{(ln(\phi_1/\phi_2))^\alpha}$$

where ϕ_1=X-ray flux measured through thinner foil

ϕ_2=X-ray flux measured through thicker foil

a and α are plasma and apparatus dependent coefficients, determined by theoretical X-ray emission calculations [10,11].

On TCA, these temperature measurements are performed by using 5 pairs of surface barrier diodes (ORTEC CA-15-100-300), with the following characteristics : surface = 100 mm^2 (circular)

Au contact layer = 0.02 μm

Si dead layer = 0.2 μm

Si active layer = 300 μm

The diodes view the plasma in a poloidal plane through a slit (pin-hole technique), and are covered with 25 or 75 μm Be foils to measure T_e at five radii in the plasma, 0, ±5.3 and ±10.6 cm. At present, the values of the coefficients used are : a=821 [eV] and α=1.481, applicable to a pure hydrogen plasma. More accurate values are under calculation, to take into account the impurity content of the plasma.

The X-ray temperatures at the different radii have been calibrated with respect to a Thomson scattering T_e profile for a typical set of shots. This is performed by means of a correction factor c that multiplies the ratio ϕ_1/ϕ_2.

In addition we use a single pair of diodes with 150 and 375 μm respectively beryllium filters. These diodes observe $\sim\pm20\%$ of the plasma diameter, viewing at 30 $^\circ$ from the vertical. The AC component of these signals is selected in two frequency ranges and used for a) sawtooth amplitude at f $\sim$ 1 kHz and b) f$>$5 kHz for mhd mode activity.

The Hard X-ray flux from the limiters is measured using an NE102A plastic scintillator plus photomultiplier combination.

e) <u>Bolometer</u>

The bolometer on TCA [12] consists of a thin Ge layer (1 μm) which has been evaporated onto a thin foil of stainless steel with 1.5 μm of MgO_2 as electrical insulation. The plasma radiation absorbed by this foil results in a change in electrical resistance of the semiconducting material which is measured through a fine gold structure evaporated onto the semiconductor.

The resistance, being of semiconducting material, follows an exponential law with respect to its temperature.

$$R(T) = R_0 \, e^{-\alpha T}$$

where R_0 : calibrated resistance value

α : temperature coefficient

The absorbed power is obtained by performing the following calculation :

$$P = c \frac{dT}{dt} + G \, T(t)$$

or

$$P = c \left(\frac{dT}{dt} + \frac{1}{\tau} T(t) \right)$$

where c : heat capacity of the detector

G : thermal conductance accounting for losses through heat diffusion and reradiation

τ : thermal relaxation time

The solution of the second equation is performed numerically.

The bolometer is a single-channel instrument and can therefore view only one chord of the plasma at a time. For spatial radiation profiles a series of 10-15 reproducible shots is needed. To unfold the experimental data, the line intensity profile is fitted by a spline-polynomial of third order. Abel's integral is then solved numerically for the derivative of this polynomial. Care has to be taken when

positive slopes occur, especially near the plasma centre. Typical profiles, both projected and inverted, are shown in Fig. 9.

f) Thomson Scattering

The electron temperature is measured by conventional Thomson scattering of ruby-laser light. The laser system (Apollo, model 35) provides, in principle, two separate pulses of ~10 J during 25 ns. The design, similar to a previously proven system [13], is shown in Fig. 10. The laser, the optical apparatus and the detection system are mounted on a trolley which can be moved between discharges to measure a temperature profile (-12 cm<y<15 cm). The beam dump is constructed with two 17 cm long blue glass plates set at the Brewster angle. The relay optics consist of three lenses and 2 notch filters. The collection lens with a diameter of 110 mm forms an image of the scattering volume on a field lens. Two notch filters positioned symmetrically with respect to the field lens are used to reduce the laser stray light. A third lens focusses the image on the entrance slit (15 mm height, 2 mm width) of a 0.5 m Spex spectrometer. The light refracted by the grating (600 or 1200 1/mm) falls on ten fibre optic channels. The photon flux from each channel is monitored by a photomultiplier, type EMI 9658 RA. The quantum efficiency of these tubes is about 9% at 7000 Å, rising to ~15% at 6300 Å and a gain of 5×10^6 can be easily achieved. The signals are then transfered to a Camac ADC.

The gains of the photomultipliers are chosen to give a signal proportional to the power input in each channel. This is performed with a calibrated tungsten ribbon lamp. Results from a typical pulse are shown in Fig. 11.

The temperature calculation [14] takes into account the relativistic effects which become important for $T_e>1$ keV.

g) Electron Cyclotron Emission

A scanning Michelson interferometer is employed on TCA to measure the plasma emission spectrum up to 1000 GHz. The system is based on a conventional vibrating mirror polarizing interferometer [15]. Radia-

tion from the equatorial plane of the plasma is transmitted by a wedged crystal quartz window and a 50 mm diameter light pipe of 1.2 m length to the spectrometer. The antenna gain has been measured to be 12, corresponding to an image of 10 cm diameter at the centre of the plasma. The detector is an InSb bolometer operating at 4.2 K. A scan can be made in 12 ms with a maximum path difference of 30 mm, corresponding to a frequency resolution of 10 GHz. Mirror displacement is either measured optically with a HeNe laser interferometer or electronically by use of the motional emf in the vibrator coil. This latter method is more reliable although it requires calibration with a fixed frequency microwave source. A typical scan and the resulting spectrum of emission in the extra-ordinary polarisation are shown in Fig. 12. Both the time and frequency resolution given above can be improved since the fringes of the interferogram are localized in the central part of the scan when the mirror is moving most rapidly.

Although the parameters of TCA are such that the plasma should be optically thick to the extraordinary mode of the second harmonic ece, the low toroidal field severly restricts its use as an electron temperature diagnostic. The upper (or right-hand) cyclotron cut-off [16] appears in the plasma when $\bar{n}_e > 2.7 \times 10^{13}$ cm^{-3}, interfering with observation of the second harmonic. The positions where observation is blocked can be determined from the density profiles measured by the FIR interferometer. These are plotted as a function of the line averaged density in Fig. 13 b). If $\bar{n}_e < 1.4 \times 10^{13}$ cm^{-3} the spectrum is completely dominated by supra-thermal emission, particularly near the plasma frequency. Thus there is only a narrow density range in which complete temperature profiles can be obtained. A further problem of the low field, and hence low emission frequencies, is the large variation in the instrumental response spectrum which particularly effects the profile on the low field side.

Fig. 14 shows the temperature profile deduced from the spectrum in Fig. 12 and another at slightly higher density, clearly showing the effects of the cut-off. It appears that the second profile in Fig. 14 is affected even at frequencies higher than cut-off, an observation that is confirmed in Fig. 13 a). Here the central ece temperature is shown to drop below that given by Thomson scattering already at densi-

ties below cut-off. This is in contrast with recent work on ASDEX [17] where refractive effects due to cut-off (calculated from assumed density profiles) were not seen to be important. An explanation may lie in the longer wavelengths of emission at low fields, and the relatively larger proportion of the plasma viewed by the TCA ece system.

h) Neutral Particle Analyser

The central ion temperature is measured by spectral analysis of the charge exchanged neutral atoms originating in the core of the plasma. The emitted flux

$$S = n_i \, n_o \, <\sigma v>_{cx} \, \frac{dn}{dE} \, \frac{d\Omega}{4\pi}$$

combined with a detector efficiency given by $\eta(E,n)$ for channel n leads to the expression, for a Maxwellian plasma,

$$T_i \sim -\left(\frac{dg(E)}{dE}\right)^{-1} \; ; \quad g(E) = \frac{S_n(E)\,\Delta E}{\sigma_{cx}\,E\,\Delta E \; \eta(E,n)}$$

The NPA used on TCA was constructed by the Ioffe Institute [18] and is shown in Fig. 15. The instrument has 5 channels with relative energies 3.7 : 2.7 : 1.9 : 1.3 : 1.0. There is a constant ratio between the energies of the different channels and the voltage applied on the electric divider U_{div} ($E_1 : U_{div}$ = 1keV:0.6kV). It is capable of both mass-dependent (E-B) and mass-independent (E-E) analysis, of which the latter is mostly used on TCA. Relative calibrations of the 5 channels was carried out using a source installed in the analyser, and then checked by sweeping the spectral range of the instrument to superimpose the 5 spectra. Only slight modifications to the channel efficiencies were needed to align the separate spectra.

The signal treatment consists of a low-level hybrid discriminator (Lecroy PC100) close to the open multiplier tube which delivers pulses into 50 Ω. The ECL output signal is then counted in the screened room following further re-shaping. The data analysis consists of a least-squares fit through selected channels as a function of time. Typical data are shown in Fig. 16. The spectrum observed is not a perfect

gaussian, being slightly concave, and the measured value of T_i depends on the spectral range chosen for analysis. In Fig. 17 we show the ion-temperature as a function of the typical range of energies used. We see that using high energy channels over-estimates T_i because the noise on these channels is a significant part of the signal. Low energy neutrals emitted by the outer plasma produce a particle excess in the low energy range, giving a too low estimation of T_i. We avoid most of these problems by restricting the analysis between 1 and 4 keV.

i) Langmuir Probe

The scrape-off layer has been investigated by means of electrical probes. A movable Langmuir probe is installed in the equatorial plane of the TCA vacuum vessel. The probe is opposite the limiters and is a 5 mm long Molybdenum wire of 0.6 mm in diameter. The probe voltage can be swept between -100 V and 100 V within about 1 ms. The probe current was measured with a current probe. The ion density is obtained from measurements of the ion saturation current (probe bias -120 V). The electron temperatures were obtained through analysis of the Langmuir probe characteristics. The analysis showed that during the ohmic heating phase the boundary plasma is maxwellian.

j) Database Treatment

Database analysis software was written for use on TCA, with records representing time-slice information during the tokamak shot. Most data are interactively verified and adjusted if necessary using cursor control. Display software allows windowing, power law combination of parameters, regression analysis and histogramming. Considerable effort was made to guarantee both flexibility and simplicity of operation.

IV. EXPERIMENTAL RESULTS

a) Raw Data

In Figure 18, we show the simplest raw data as a function of line-averaged density for both hydrogen and deuterium as working gases, namely :

a) plasma column resistance R_{pl},

b) peak electron temperature $T_e(0)$ using Thomson scattering,

c) central ion temperature $T_i(0)$,

d) line-integrated radiated power $\int P_{rad} dl$,

e)f)g) line-integrated line emission of $H_\alpha + D_\alpha$, OII, FeII,

h) $\beta + l_i/2$,

j) $\beta_\perp$ as measured by the diamagnetic loop,

k)l) edge temperature and ionisation current from Langmuir probe measurements.

b) Density Profiles

The symmetric Abel inversions of the FIR 8 channel interferometer measurement for both low and high density discharges are shown in Fig. 19 a). One can notice on the normalised profiles $n_e(r)/n_e(0)$ that increasing the density tends to peak its profile (Fig. 19 b)). This fact is confirmed over the full density range by the plot of the half width at half maximum (Fig. 20) without any difference between hydrogen and deuterium discharges.

Such a density profile behaviour is different from that normally seen on larger tokamaks, but has been observed in Alcator A [19]. In particular, the following scaling has been proposed by them :

$n_e(r) = n_e(0)(1-r^2/a^2)^{\kappa_n}$ where $\kappa_n = 0.5 + 0.025 \, \bar{n}_{e13}$ for $10 < \bar{n}_{e13} < 60$, $I_p = 150$ kA and $B_\phi = 60$ kG. Small circular Doublet III discharges ($a = 23$ cm, $I_p = 120$ kA, $B_\phi = 24$ kG) [20] also show that the shape parameter α_n of the density profile $n_e(r) = n_e(0)[0.95(1-r^2/a_p^2)^{\alpha_n} + 0.05]$,

where $a_F=44$ cm, increases from 5 to 8 when $\bar{n}_{el\,3}$ varies from 3 to 9. FT density profiles are also available [21] and, if restricted to values of the safety factor from 3 to 4, they tend to peak at higher densities.

We find that all the results can be matched together if they are plotted versus the Murakami parameter $n_e(0)R_0/B_\phi$. Fig. 20 shows both the half width at half maximum normalized to minor radius and the peaking factor κ_n versus this parameter, and one can see that the Alcator A scaling can be extended to include all these small radius tokamaks with $3<q<4$ as

$$K_n = 0.75 + 1.3 \times 10^{-15} n_e(0) R_0 / B_\phi \quad [cm, kG]$$

The correlation coefficient is 0.77 if data from FT is excluded.

Although the Murakami parameter does provide an efficient linking of the data from these tokamaks it does suggest a dependance on B_ϕ not seen in other machines [19]. Since we have used constant q perhaps a scaling with $n_e(0)a^2/I_p$ would be more appropriate because a peaking of the profile as the plasma current is decreased has been observed elsewhere [19].

c) Impurities

We note that the electron temperature (Thomson) tends to decrease only marginally with increasing density, and that the column resistance increases slightly. In Fig. 21 a) we show the value of $Z_{eff}(0)$, assuming $q(0)=0.9$ for all densities, calculated as

$$Z_{eff}(0) = 1.84 \times 10^{-4} T_e^{3/2}(0) \frac{V_R}{B_\phi} - 0.755 \quad [eV, V, kG]$$

and we notice, particularly in hydrogen, a continuous reduction as the density is increased.

In the core the radiation losses come mainly from heavy impurities and follow $P_{rad} \sim n_e\, n_I\, f(T_e)$, where n_I is the impurity

where $a_F=44$ cm, increases from 5 to 8 when $\bar{n}_{el3}$ varies from 3 to 9. FT density profiles are also available [21] and, if restricted to values of the safety factor from 3 to 4, they tend to peak at higher densities.

We find that all the results can be matched together if they are plotted versus the Murakami parameter $n_e(0)R_0/B_\phi$. Fig. 20 shows both the half width at half maximum normalized to minor radius and the peaking factor κ_n versus this parameter, and one can see that the Alcator A scaling can be extended to include all these small radius tokamaks with $3<q<4$ as

$$K_n = 0.75 + 1.3 \times 10^{-15} n_e(0)R_0/B_\phi \quad [cm, kG]$$

The correlation coefficient is 0.77 if data from FT is excluded.

Although the Murakami parameter does provide an efficient linking of the data from these tokamaks it does suggest a dependance on B_ϕ not seen in other machines [19]. Since we have used constant q perhaps a scaling with $n_e(0)a^2/I_p$ would be more appropriate because a peaking of the profile as the plasma current is decreased has been observed elsewhere [19].

c) Impurities

We note that the electron temperature (Thomson) tends to decrease only marginally with increasing density, and that the column resistance increases slightly. In Fig. 21 a) we show the value of $Z_{eff}(0)$, assuming $q(0)=0.9$ for all densities, calculated as

$$Z_{eff}(0) = 1.84 \times 10^{-4} T_e^{3/2}(0) \frac{V_R}{B_\phi} - 0.755 \quad [eV, V, kG]$$

and we notice, particularly in hydrogen, a continuous reduction as the density is increased.

In the core the radiation losses come mainly from heavy impurities and follow $P_{rad} \sim n_e n_I f(T_e)$, where n_I is the impurity

density. Taking the heavy impurities to be iron, f is then a weak function in the T_e range observed on TCA and we numerically estimate their concentration as

$$\eta_{metal}(0) = \frac{n_{metal}(0)}{n_e(0)} = 6.41 \times 10^{-7} \frac{P_{rad}[W]}{n_{e13}^2(0)}$$

To obtain $P_{rad}(0)$ we have assumed that P_{rad} has a flat profile. Since this is fairly true (Fig. 9), the error in not having measured $P_{rad}(r)$ for all densities is probably only small. We see in Fig. 21 b) that $\eta_{metal}(0)$ drops rapidly with density to less than 0.2%. From this we can go further and estimate the concentration of light impurities, assumed to be oxygen, as

$$\eta_{light}(0) = \frac{n_{light}(0)}{n_e(0)} = \frac{Z_{eff}(0) - 1 - 380 \eta_{metal}(0)}{56}$$

in which the core ionisation states are chosen as $Z_{metal} \sim 20$ and $Z_{light} \sim 8$. The result is plotted in Fig. 21 c), where the rather large scattering comes essentially from the uncertainty on $Z_{eff}(0)$, itself due to the statistical error on $T_e(0)$.

The working gas ion density is then calculated as

$$\frac{n_i}{n_e} = 1 - 8\eta_{light} - 20\eta_{metal}.$$

For densities $\bar{n}_{e13} > 2.5$ we find that $n_i/n_e > 80\%$.

d) Plasma Energy and Confinement Time

In order to calculate the plasma energy content we must know the temperature profiles, which are assumed to be $T_i(r) = T_{io}(1-r^2/a^2)^{\kappa_{Ti}}$ and $T_e(r) = T_{eo}(1-r^2/a^2)^{\kappa_{Te}}$. κ_{Ti} is set equal to 1.0, the value found with an ion power balance simulation with neo-classical thermal diffusivity enhanced by an anomalous factor of 2, and κ_{Te} to 2.5 which is in agreement with ece measurements around $\bar{n}_{e13} = 2.5$ and consistent with the calculated current density profile (see section IV e)). T_{eo}, T_{io} and $n_e(r)$ are measured quantities.

density. Taking the heavy impurities to be iron, f is then a weak function in the T_e range observed on TCA and we numerically estimate their concentration as

$$\eta_{metal}(0) = \frac{n_{metal}(0)}{n_e(0)} = 6.41 \times 10^{-7} \frac{P_{rad}[W]}{n_{e13}^2(0)}$$

To obtain $P_{rad}(0)$ we have assumed that P_{rad} has a flat profile. Since this is fairly true (Fig. 9), the error in not having measured $P_{rad}(r)$ for all densities is probably only small. We see in Fig. 21 b) that $\eta_{metal}(0)$ drops rapidly with density to less than 0.2%. From this we can go further and estimate the concentration of light impurities, assumed to be oxygen, as

$$\eta_{light}(0) = \frac{n_{light}(0)}{n_e(0)} = \frac{Z_{eff}(0) - 1 - 380\,\eta_{metal}(0)}{56}$$

in which the core ionisation states are chosen as $z_{metal} \sim 20$ and $z_{light} \sim 8$. The result is plotted in Fig. 21 c), where the rather large scattering comes essentially from the uncertainty on $Z_{eff}(0)$, itself due to the statistical error on $T_e(0)$.

The working gas ion density is then calculated as

$$\frac{n_i}{n_e} = 1 - 8\eta_{light} - 20\eta_{metal}.$$

For densities $\bar{n}_{e13} > 2.5$ we find that $n_i/n_e > 80\%$.

d) Plasma Energy and Confinement Time

In order to calculate the plasma energy content we must know the temperature profiles, which are assumed to be $T_i(r)=T_{io}(1-r^2/a^2)^{\kappa T_i}$ and $T_e(r)=T_{eo}(1-r^2/a^2)^{\kappa T_e}$. κ_{T_i} is set equal to 1.0, the value found with an ion power balance simulation with neo-classical thermal diffusivity enhanced by an anomalous factor of 2, and κ_{T_e} to 2.5 which is in agreement with ece measurements around $\bar{n}_{e13}=2.5$ and consistent with the calculated current density profile (see section IV e)). T_{eo}, T_{io} and $n_e(r)$ are measured quantities.

We calculate

$$W_e = \frac{3}{2} e \int n_e T_e \, dV$$

$$W_i = \frac{3}{2} e \left(1 - 8\eta_{light} - 20\eta_{metal}\right) \int n_e T_i \, dV$$

$$W_{light} = \frac{3}{2} e \, \eta_{light} \int n_e T_i \, dV$$

$$W_{metal} = \frac{3}{2} e \, \eta_{metal} \int n_e T_i \, dV$$

$$W_{tot} = W_e + W_i + W_{light} + W_{metal}$$

in which we assume that the impurity ion temperature is equal to the hydrogenic ion temperature everywhere, due to the small energy transfer time between these species, and that the impurity concentrations have flat profiles. This latter assumption is also consistent with the current density profile calculated in section IV e).

W_e, W_i and W_{tot} are plotted in Figure 22. The fact that W_e is greater in deuterium and that W_i is greater in hydrogen may partially be explained by the proportionality between the electron-ion equilibration power P_{ei} and $1/A_i$, where A_i is the ionic mass.

We then calculate the global energy confinement times $\tau_{Ee} = W_e/P_{oh}$ and $\tau_E = W_{tot}/P_{oh}$, shown in Figures 23 a) and b) respectively. The usual linear dependance on the line averaged density is immediately apparent, although τ_{Ee} for hydrogen appears to saturate at higher densities when anomalous ion transport becomes an important energy loss mechanism. It is of interest to compare the TCA results with some of the popular scaling laws for ohmically heated plasmas. In Figure 23 b) we show the prediction of the original Alcator A-INTOR scaling as modified by TFR [22]

$$\tau_E = 5.0 \times 10^{-21} \, \bar{n}_e \, a^2 \, R_0 \, q^{0.5} \quad [s, cm]$$

and the neo-Alcator scaling presented by Goldston [23]

$$\tau_E = 7.1 \times 10^{-22} \, \bar{n}_e \, a^{1.04} \, R0^{2.04} \, q^{0.5}.$$

The former law seems to describe the TCA data better, the latter

actually predicting a lower confinement time by a factor of 0.2 (a/R_0) if it is rewritten (valid for PLT) as

$$\tau_E = 1.0 \times 10^{-21} \ \bar{n}_e \ a \ R_0{}^2 \ q^{0.5}.$$

Equivalently for τ_{Ee} the TCA data is best approximated by an Alcator A type scaling. In Figure 23 a) we show the scaling law produced by minor radius scaling experiments on Doublet III [20], (corrected for major radius dependance)

$$\tau_{Ee} = 2.5 \times 10^{-21} \ \bar{n}_e \ a^2 \ R_0 \ q^{0.75}$$

and the Pfeiffer Waltz scaling [24] constrained to geometrical parameters

$$\tau_{Ee} = 5.6 \times 10^{-22} \ \bar{n}_e \ a^{1.25} \ R_0{}^2.$$

Clearly TCA falls into the data set best represented by an $a^2 R_0$ scaling, with confinement times higher than those given by an $a R_0{}^2$ scaling due to its relatively small aspect ratio. An aspect ratio of 5 would make the two scalings equivalent both for τ_E and τ_{Ee}. By varying the profiles used in the calculation of W_e and W_i we have found that it is only by replacing the measured relatively flat density profiles with an analytic profile with $\kappa_n \sim 1.5$ that the confinement times can be reduced significantly. This is not compatible with the profiles obtained by the multi-channel interferometer, as described in Section IV b). Adding a pedestal of 30 eV to the temperature profiles or imposing $T_i(r) < T_e(r)$ does not change the estimate of τ_E by more than 10%.

e) Electron Power Balance

To perform a radial electron power balance, one has to know the current density profile. Therefore we assume that the Z_{eff} profile has the form : $Z_{eff}(r)=1+\left(Z_{eff}(0)-1\right)\left(1-r^2/a^2\right)^{\kappa Z_{eff}}$. The current density is then calculated with classical Spitzer resistivity (no trapping correction) and constant parallel electric field. κ_{T_e} and $\kappa_{Z_{eff}}$ are chosen to match the following conditions :

a) the safety factor at the centre should be 0.9.

b) the assumed Z_{eff} profile should correspond to the profile determined by a simulation assuming coronal equilibrium [25]. This is achieved with impurity concentrations η_{light} and η_{metal} that are constant throughout the plasma (Fig. 24).

Under these conditions, κ_{T_e} and $\kappa_{Z_{eff}}$ are tied variables and the only reasonable solution is around $\kappa_{T_e} = 2-2.5$ and $\kappa_{Z_{eff}} = 1-2$. Within this range, the following analysis is rather insensitive to the choice made.

Then the power balance equation

$$P_{oh} = P_{ei} + P_{rad} - \frac{1}{r}\frac{d}{dr}\left(r\,(n_e \chi_e)\,e\,\frac{dT_e}{dr}\right)$$

is solved, neglecting convection losses, in order to get the value of the thermal diffusivity χ_e. The result for a deuterium discharge with $\bar{n}_{el3} = 2.6$ is shown in Figure 25. The value at half radius of $n_e \chi_e$ is plotted in Figure 26 versus the central density for both working gases (hydrogen points suffer a large error because of the difficulty in estimating P_{ei} when T_i is close to T_e). We can note in deuterium that $n_e \chi_e$ tends to decrease with increasing density. Also shown on this figure is the standard INTOR scaling

$$\chi_e = 5 \times 10^{17}/n_e \; [cm,s].$$

Here again the scaling used for INTOR produces a better representation of the data. The χ_e scaling proposed by Goldston [23] gives a value 3 times that seen in the TCA data.

V. CONCLUSION

The characteristics of the ohmic TCA target plasma used for Alfvén Wave Heating experiments have been studied. The toroidal field and plasma current were held fixed at the standard conditions ($B_\phi = 15.2$ kG, $I_p = 133$ kA, $q(a)=3$) and both the working gas and the density varied.

a) the safety factor at the centre should be 0.9.

b) the assumed Z_{eff} profile should correspond to the profile determined by a simulation assuming coronal equilibrium [25]. This is achieved with impurity concentrations η_{light} and η_{metal} that are constant throughout the plasma (Fig. 24).

Under these conditions, κ_{T_e} and $\kappa_{Z_{eff}}$ are tied variables and the only reasonable solution is around $\kappa_{T_e}=2-2.5$ and $\kappa_{Z_{eff}}=1-2$. Within this range, the following analysis is rather insensitive to the choice made.

Then the power balance equation

$$P_{oh} = P_{ei} + P_{rad} - \frac{1}{r}\frac{d}{dr}\left(r\,(n_e \chi_e)\,e\,\frac{dT_e}{dr}\right)$$

is solved, neglecting convection losses, in order to get the value of the thermal diffusivity χ_e. The result for a deuterium discharge with $\bar{n}_{el3}=2.6$ is shown in Figure 25. The value at half radius of $n_e\chi_e$ is plotted in Figure 26 versus the central density for both working gases (hydrogen points suffer a large error because of the difficulty in estimating P_{ei} when T_i is close to T_e). We can note in deuterium that $n_e\chi_e$ tends to decrease with increasing density. Also shown on this figure is the standard INTOR scaling

$$\chi_e = 5 \times 10^{17}/n_e \;[cm,s].$$

Here again the scaling used for INTOR produces a better representation of the data. The χ_e scaling proposed by Goldston [23] gives a value 3 times that seen in the TCA data.

V. CONCLUSION

The characteristics of the ohmic TCA target plasma used for Alfvén Wave Heating experiments have been studied. The toroidal field and plasma current were held fixed at the standard conditions $(B_\phi=15.2 \text{ kG}, I_p=133 \text{ kA}, q(a)=3)$ and both the working gas and the density varied.

The available set of diagnostics allows us to determine the density dependance of the macroscopic plasma parameters and to perform more detailed analysis.

We observe that increasing the density gives more peaked density profiles. Although the opposite behaviour is displayed on large tokamaks, this is compatible with small tokamak observations ($a \leqslant 23$ cm, $3 \leqslant q(a) \leqslant 4$) and summarized by the following law :

$$\kappa_n = 0.75 + 0.013 \; n_{el3}(0) \; R_0/B_\phi \, .$$

We estimate the plasma impurity content and find that the central metal concentration drops rapidly with density to less than 0.2% at $\bar{n}_{el3}=2.5$. Typical light impurities concentration is 3% over the whole density range.

TCA global energy confinement time follows the typical proportionality with the line density. Comparison with published scaling laws shows that the predictions of an original Alcator type $a^2 R_0$ scaling provide the best representation of the data; more modern $a R_0^2$ laws underestimating the observed confinement times due to the relatively small aspect ratio of TCA.

The continuous effort made to improve the plasma purity has reduced the radiated power to very small values ($P_{rad}(0)/P_{oh}(0) \sim$ 5%). This small contribution of P_{rad} to the electron power balance allows us to safely estimate the electron thermal conduction $n_e \chi_e$. We notice that $n_e \chi_e$ drops from 4×10^{17} $cm^{-1}s^{-1}$ to 2×10^{17} $cm^{-1}s^{-1}$ when $\bar{n}_e$ is increased from 0.5×10^{13} cm^{-3} to 5×10^{13} cm^{-3}.

The results presented here will serve as a basis for comparison with future plasma conditions and for the study of the plasma during Alfvén Wave Heating.

ACKNOWLEDGEMENTS

REFERENCES

[1] A.D. Cheetham et al., in Fusion Technology 1980 (Proc. 11th Symp. Oxford, 1980), Vol. 1, Pergamon, Oxford (1981) 601

[2] A. de Chambrier et al., in Plasma Physics and Controlled Nuclear Fusion research 1982 (Proc. 9th Int. Conf., Baltimore, 1982), Vol. 2, IAEA, Vienna (1983) 81
A. de Chambrier et al., Plasma Phys. 25 (1983) 1021

[3] R. Behn et al., in Controlled Fusion and Plasma Physics (Proc. 11th Europ. Conf., Aachen 1983) Vol. 7D, EPS (1983) II 471
A. de Chambrier et al., in Heating in Toroidal Plasmas (Proc. 4th Int. Symp. Rome, 1984), Vol. 2, Int. School Plasma Phys. Varenna (1984) 179
R. Behn et al., Plasma Phys. Contr. Fusion 26 (1984) 173

[4] J.B. Lister, R.W. Means and Ph. Oberson, Rev. Sci. Instrum. 53 (1982) 600

[5] D. Veron, Optics Communications 10 (1974) 95

[6] Y. Yasutomo, K. Miyata, S.I. Himenu, T. Enuto, Y. Osuwa, IEEE Transactions on Plasma Science, Vol. PS-9, nr 1 (1981)

[7] W. Barr, J. Opt. Soc. An. 52 (1962) 885

[8] F.C. Jahoda et al., Phys. Rev. 119 (1960) 843

[9] W.J. Karzas, Letter R., Astroph. J. Suppl. 6 (1961) 167

[10] D.A. Marty et al., report EUR-CEA-FC-969, July 1978

[11] P. Smeulders, report IPP 2/233, January 1979

[12] H. Jaeckel et al., Proc. D.P.G., München 1978
H. Jaeckel et al., Proc. D.P.G., Bielefeld 1980

[13] R. Prentice, Culham Report CLM-R 179 (1978)

[14] M. Mattioli, R. Papoular, Plasma Physics 17 (1975) 165

[15] A.E. Costley and J. Chamberlain, Proc. Conf. on Precision Electromagnetic Measurements, IEE Nr 113, 210, London (1974)

[16] I.H. Hutchinson and D.S. Komm, Nucl. Fusion 17 (1977) 1077

[17] D.J. Campbell and A. Eberhagen, Plasma Phys. and Controlled Fusion 26 (1984) 689

[18] V.V. Afrosimov et al., Sov. Phys. Tech. Phys. 20 (1975) 1

[19] B. Coppi, N. Sharky, Nucl. Fusion 21 (1981) 1363

[20] S. Ejima et al., Nucl. Fusion 22 (1982) 1627

[21] The FT Group, CNEN Report 80.10 (1980)

[22] Equipe TFR, Nucl. Fusion 20 (1980) 1227

[23] R.J. Goldston, Plasma Phys. Contr. Fusion 26 (1984) 87

[24] W. Pfeiffer and R.E. Waltz, Nucl. Fusion 19 (1979) 51

[25] F. Hofmann et al., Lausanne Report LRP 230/83 (1983)

FIGURE CAPTIONS

1. Cross-section of the TCA vacuum vessel.

2. Mass-spectral analysis of the background gas in TCA.
   a) after pumping
   b) after cleaning in H_2
   c) after cleaning in D_2
   d) after a discharge in H_2
   e) after a discharge in D_2

3. Pump-down curves after a tokamak discharge.

4. Traces from a typical TCA discharge.

5. Layout of diagnostics on TCA.

6. Multi-channel FIR interferometer traces.

7. Inverted density profile from multichannel FIR interferometer.

8. Sensitivity of inverted density profile to the edge profile assumptions.

9. Projected and inverted radiated power profiles.

10. Layout of the Thomson scattering system.

11. Typical Thomson scattering data.

12. Typical ece interferogram and resulting emission spectrum.

13. a) Central temperatures measured by Thomson scattering and ece.
    b) Density limit to the ece T_e diagnostic using 2nd harmonic.

14. Electron temperature profiles from ece measurements at different densities.

15. Layout of the 5-channel Neutral Particle Analyzer [18].

16. Typical data from the NPA.

17. Energy range used for NPA analysis.

18. Raw data for both H_2 and D_2 discharges :
    a) Plasma column resistance
    b) Electron temperature
    c) Ion temperature

    d) Line-integrated radiated power

    e) $H_\alpha + D_\alpha$ emission

    f) OII (4415 Å) emission

    g) FeII (2599 Å) emission

    h) $\beta + li/2$

    j) β_{DIAM}

    k) Edge temperature

    l) Edge ionisation current.

19. Typical density profiles for both low and high density discharges.

20. Half width at half maximum of the density profiles versus $n_e(0)R_0/B_\phi$ for TCA and other tokamaks.

21. a) $Z_{eff}(0)$ as a function of density.

    b) An estimate of the metal concentration.

    c) An estimate of the light impurity concentration.

22. Stored electron energy (W_e), stored ion energy (W_i) and total stored energy (W_{tot}) as a function of density.

23. a) Global electron energy confinement time as a function of density.

    b) Global confinement time as a function of density.

24. Simulated Z_{eff} profile assuming coronal equilibrium.

25. Radial electron power balance :

        a) Plasma parameters profiles

        b) Local powers

        c) Integrated powers

        d) Thermal conduction profile.

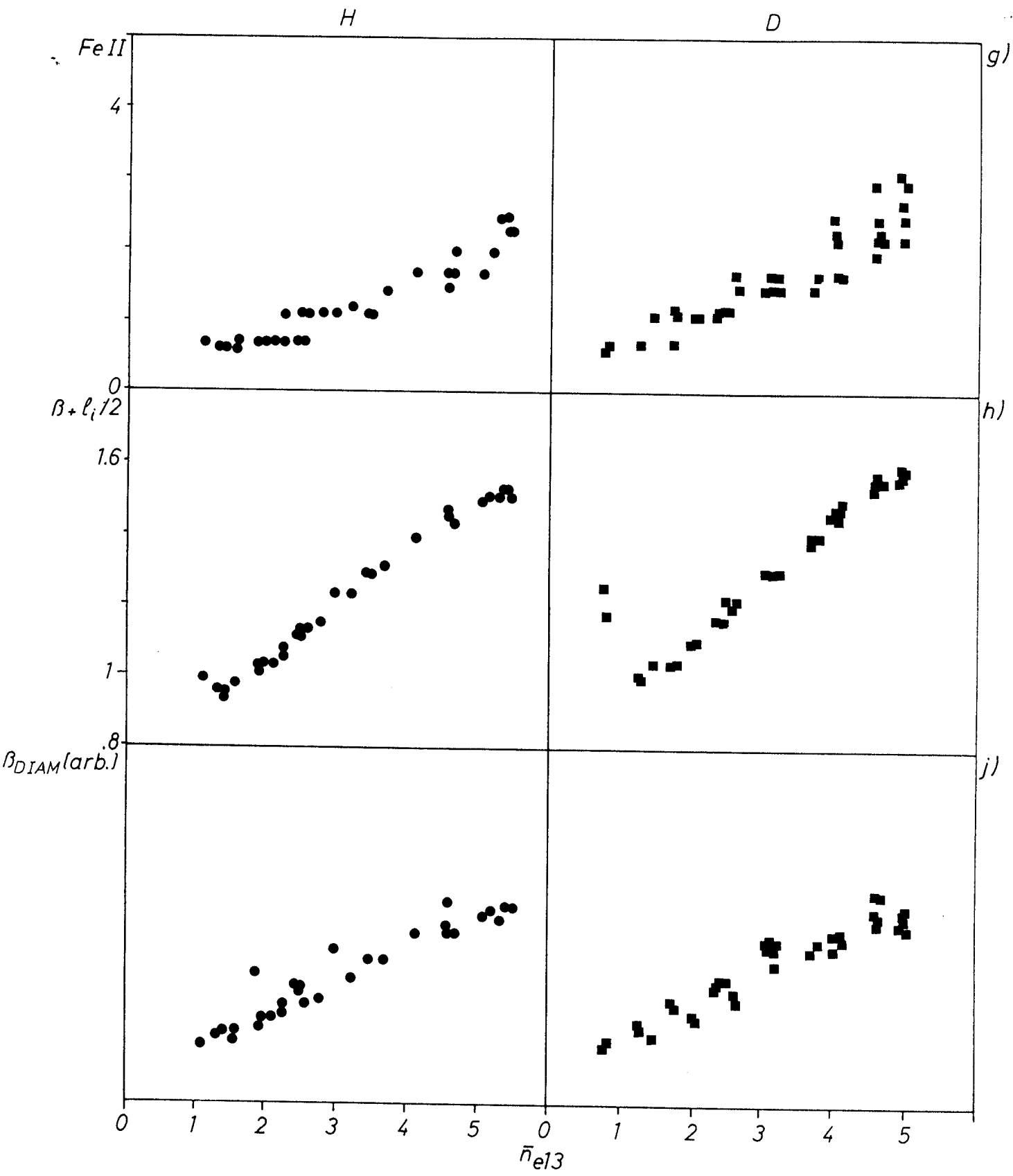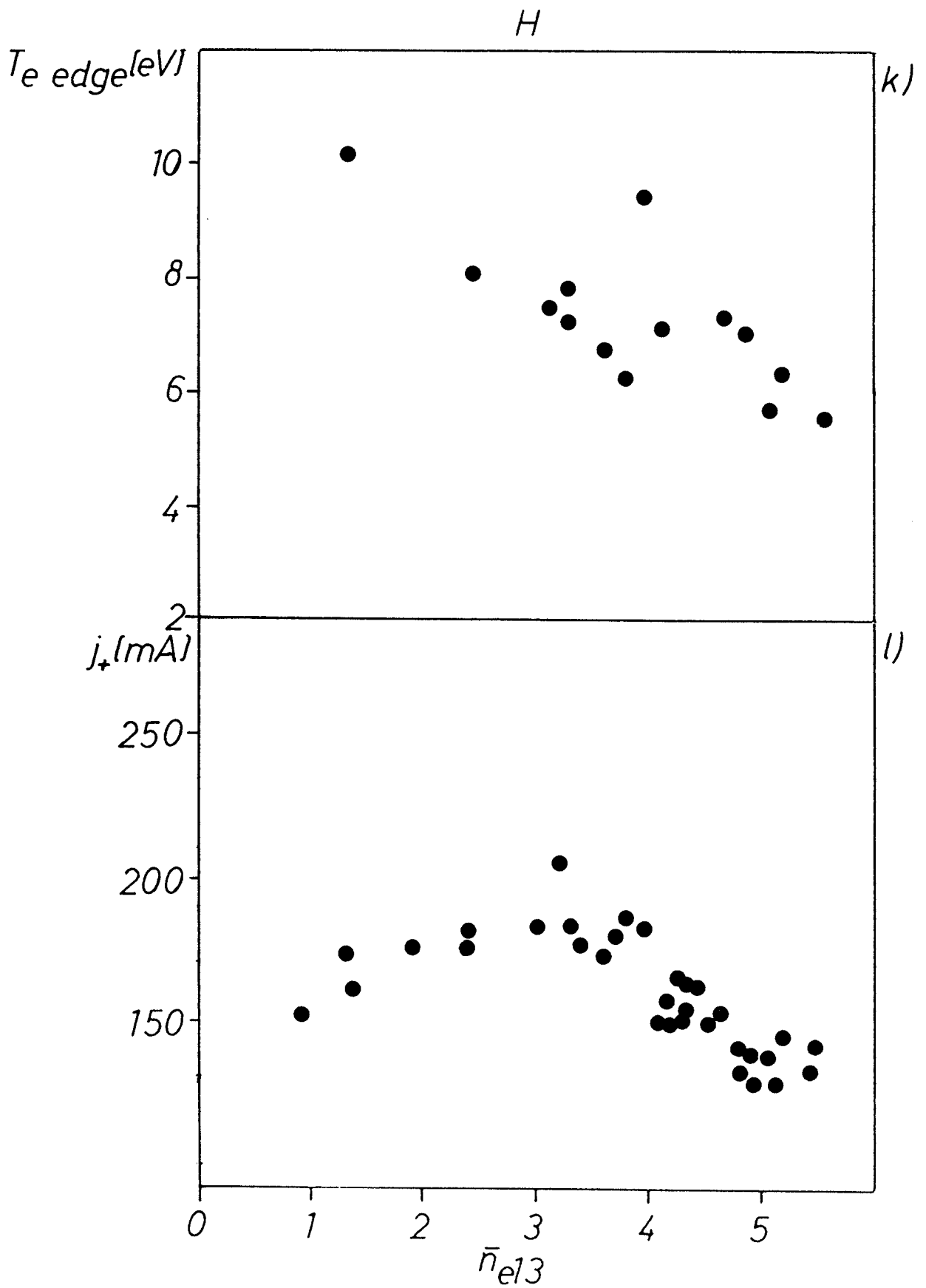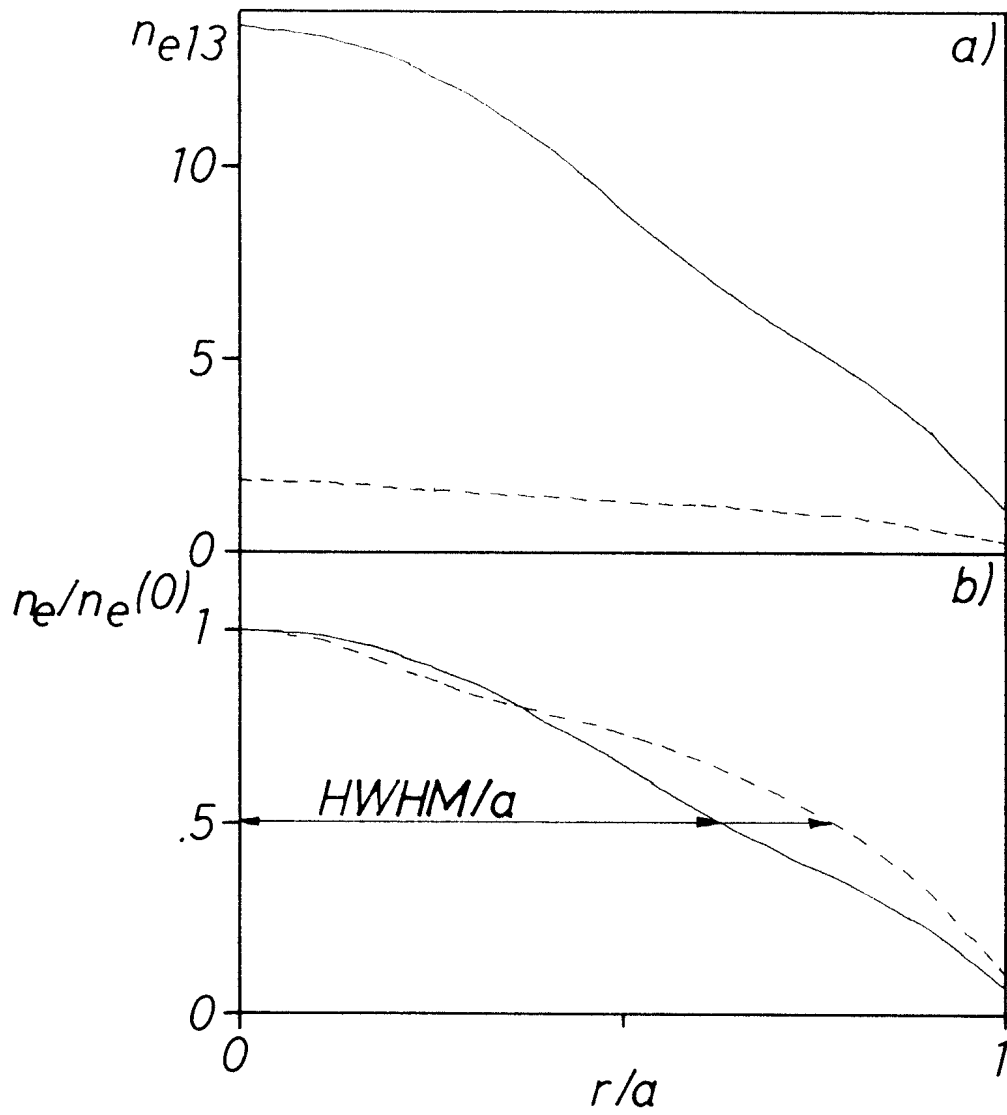26. $n_e \chi_e$ at $r = a/2$ versus central density.

1 antennae
2 ceramic insulation

333

R 615
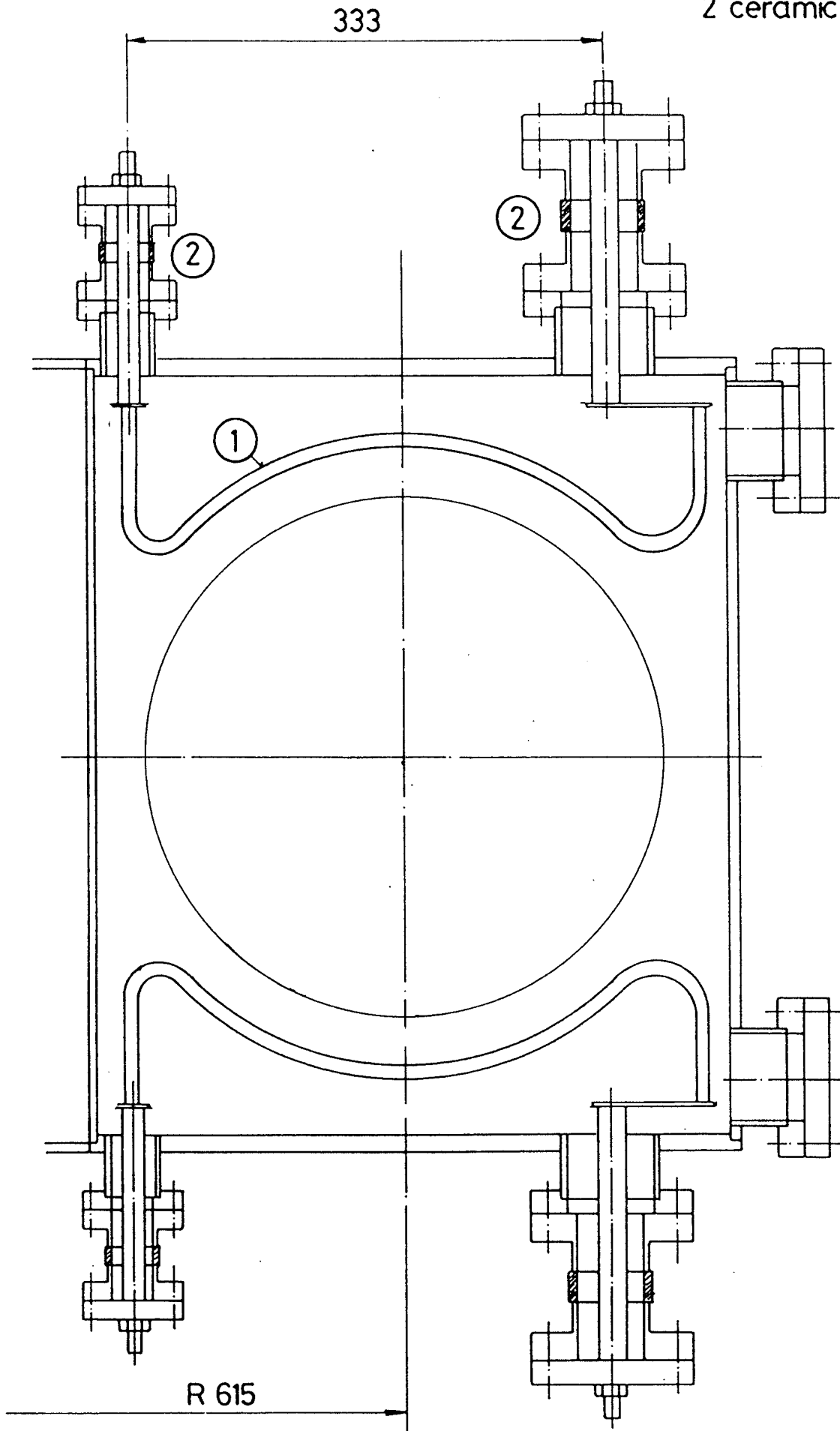
poloidal section

FIGURE 1
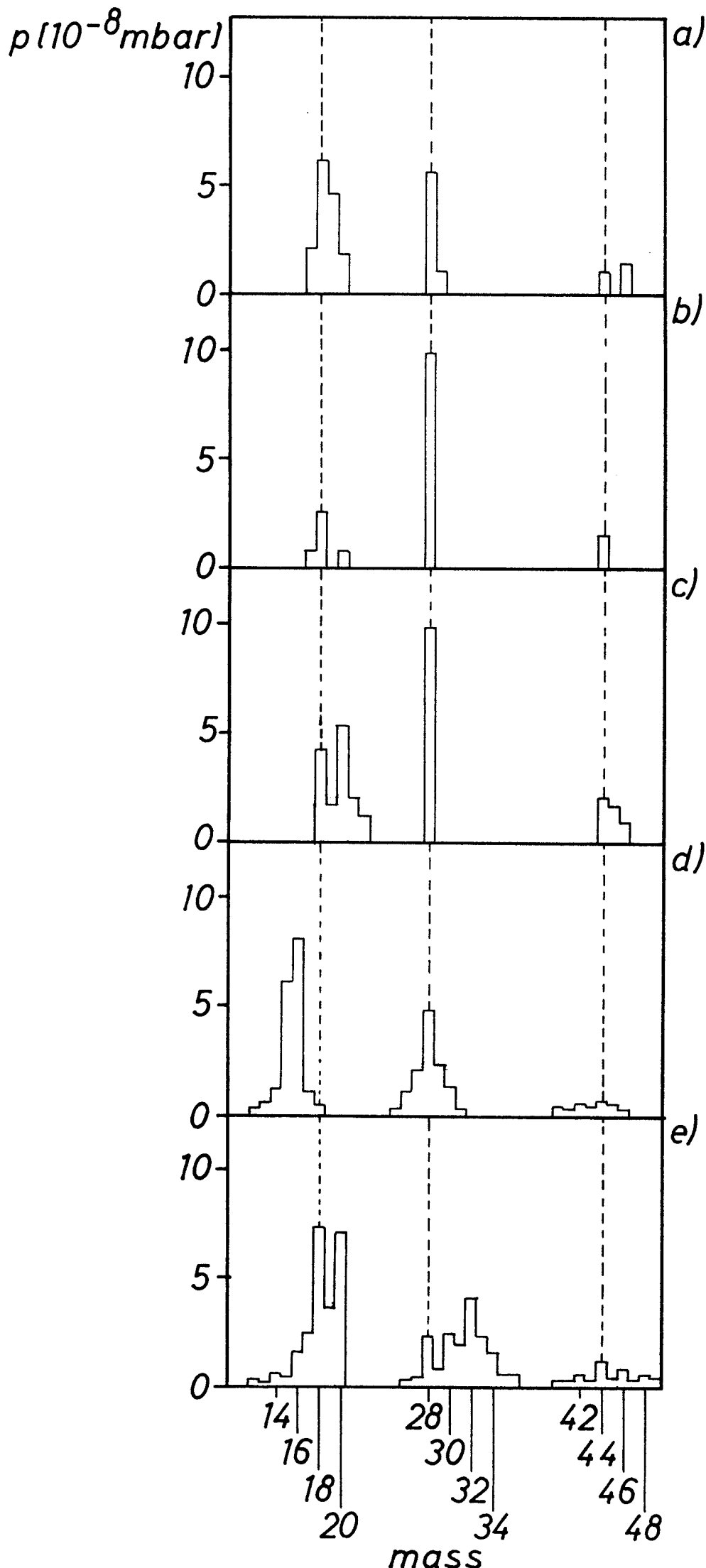
FIGURE 2
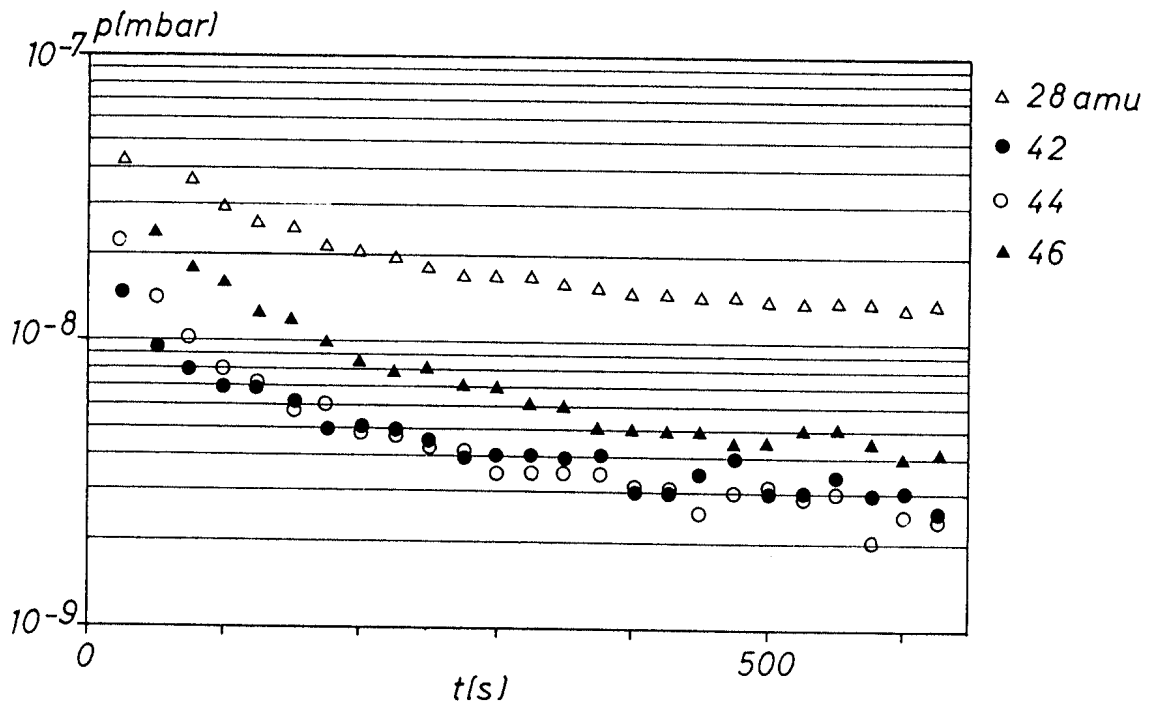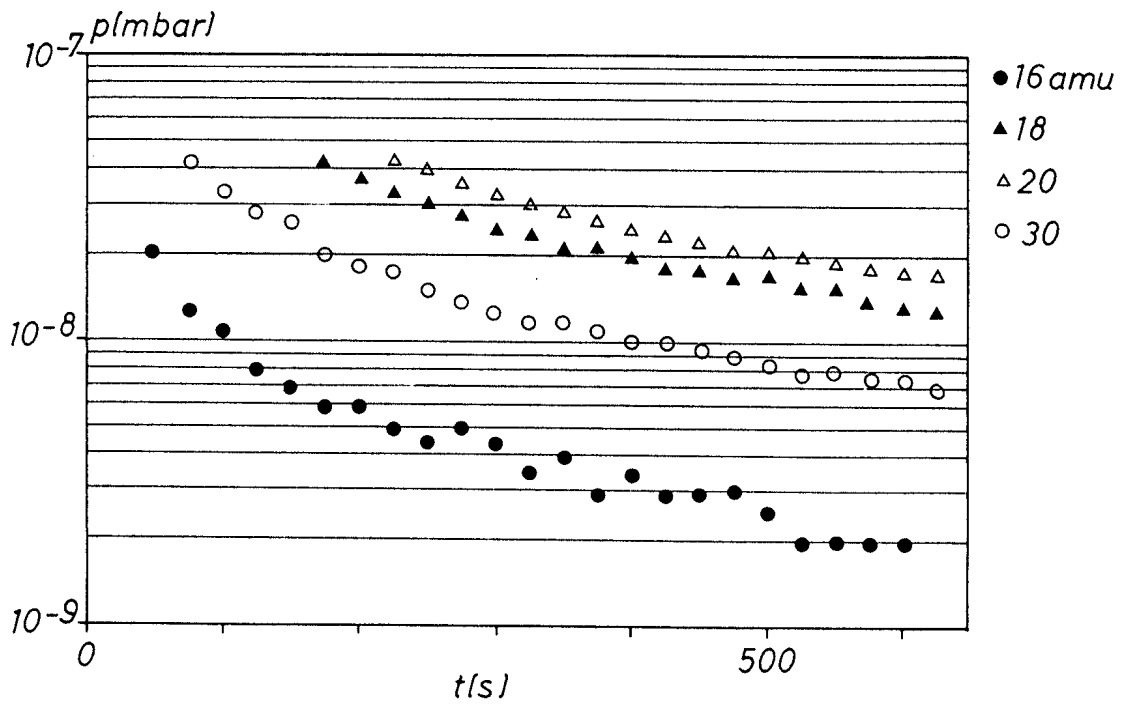
FIGURE 3
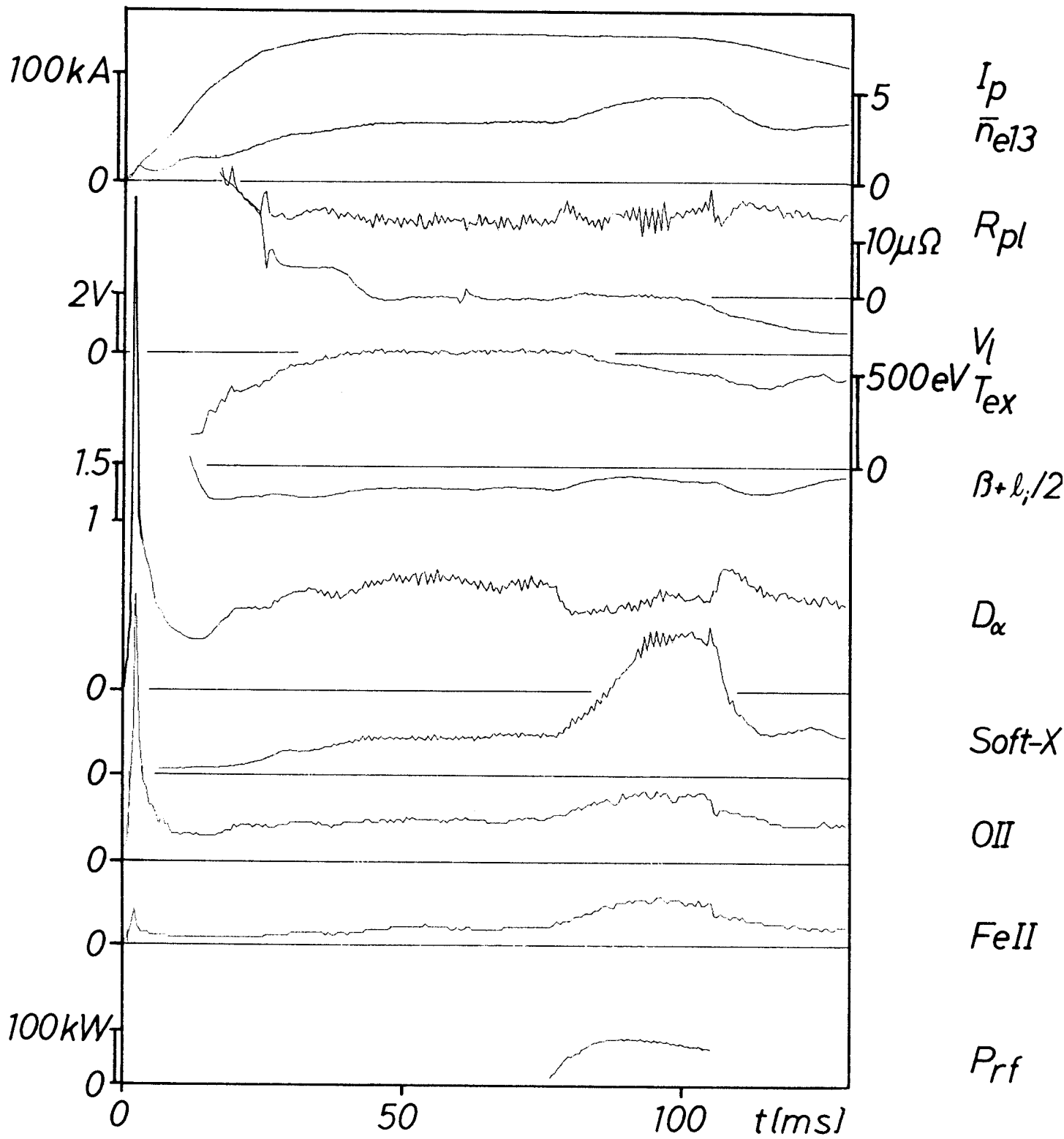
FIGURE 4
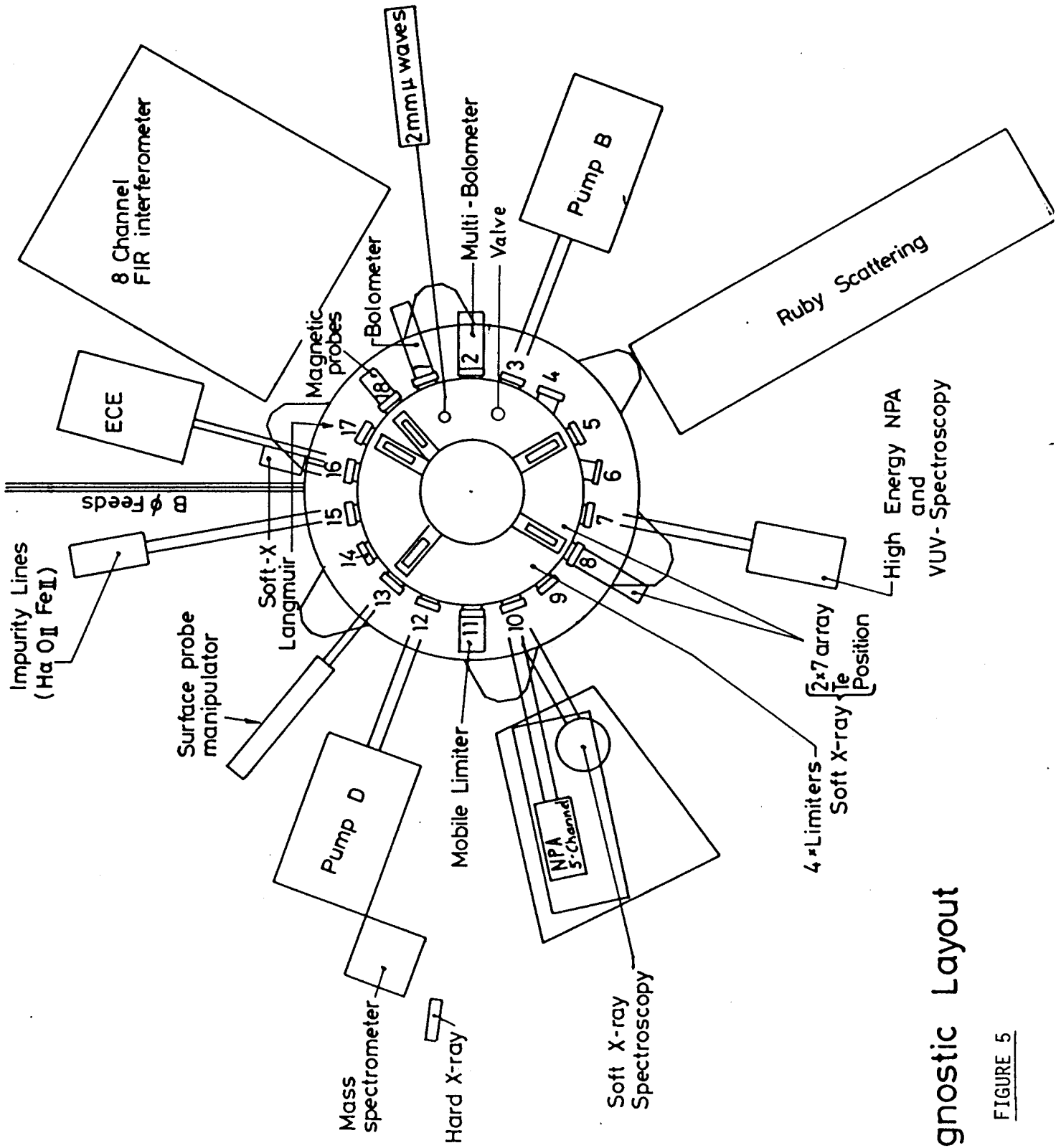
Diagnostic Layout

FIGURE 5

17583

$2\tilde{n} \stackrel{.}{=} 2 \times 10^{15} cm^{-2}$

FIGURE 6

17583

2.5 ms

n_{e13}

$t[ms]$

r/a
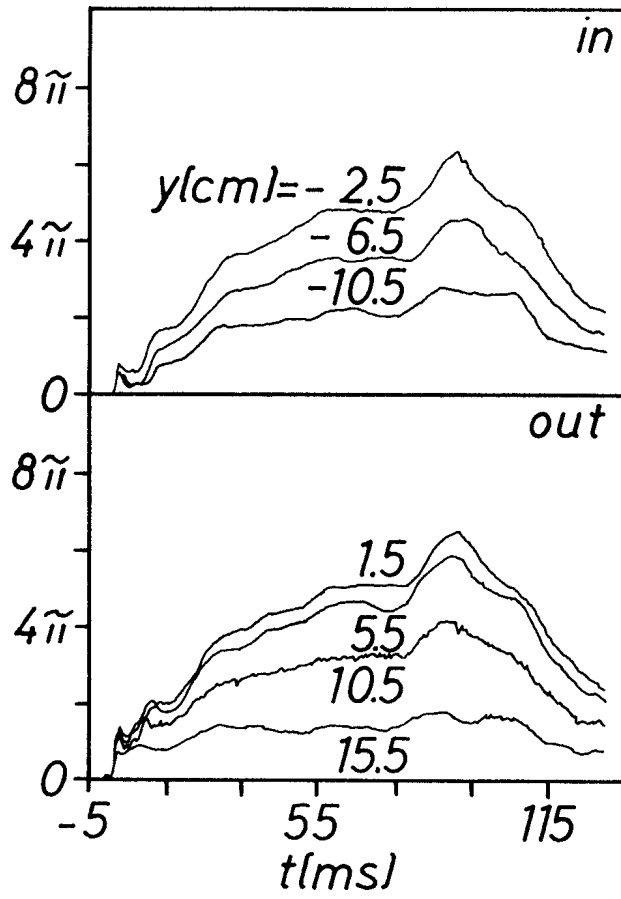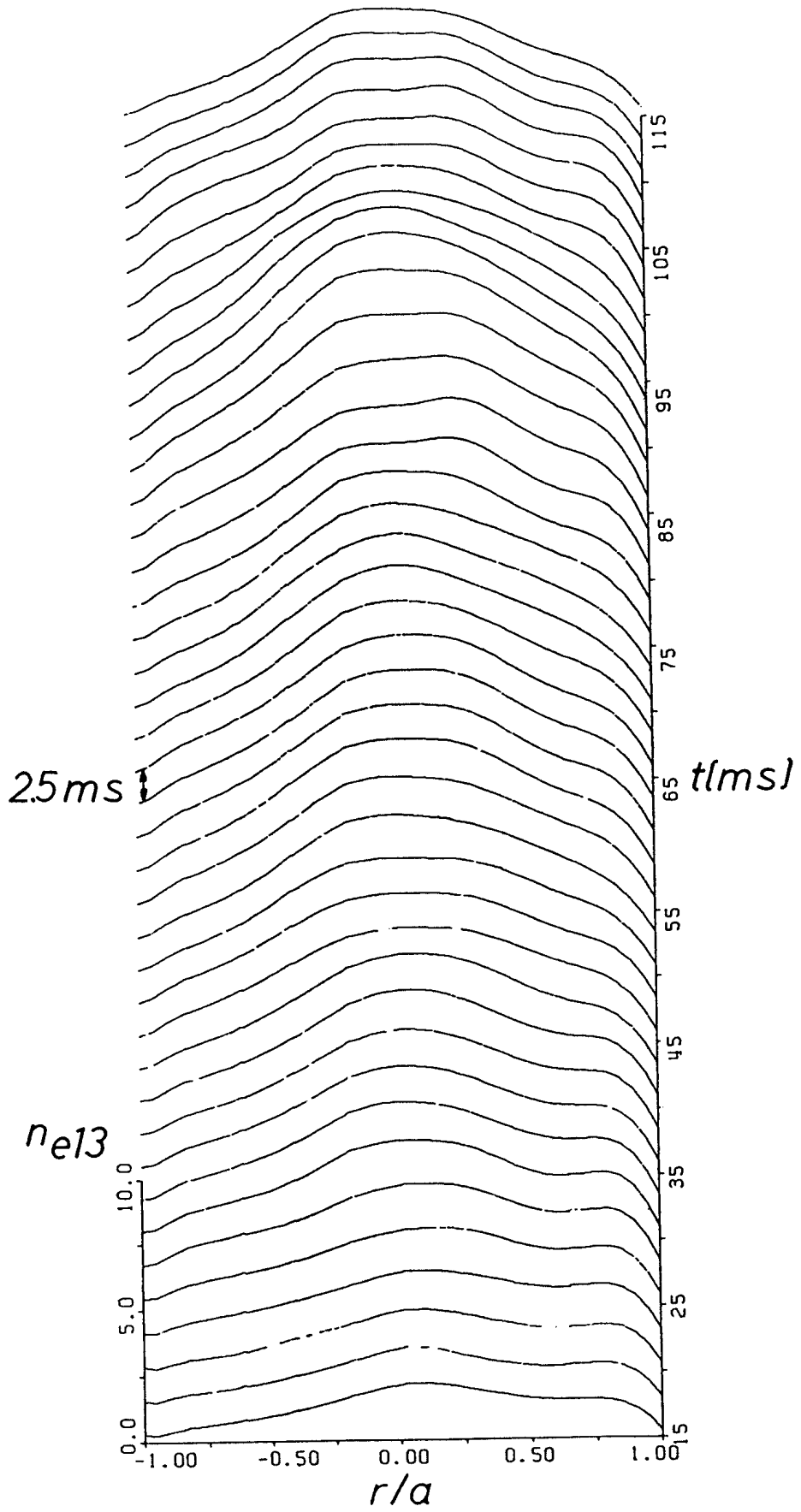
FIGURE 7

FIGURE 8

FIGURE 9

Focusing Prism

Ruby Laser

Spex
Spectrometer

Photomultipliers

Rack

Frame

Trolley

Relay Optics
and Notch Filter

Motor

Collection
Lens

Plasma

Beam Dump

0.5 m.

0

FIGURE 10

FIGURE 11

path difference(mm)
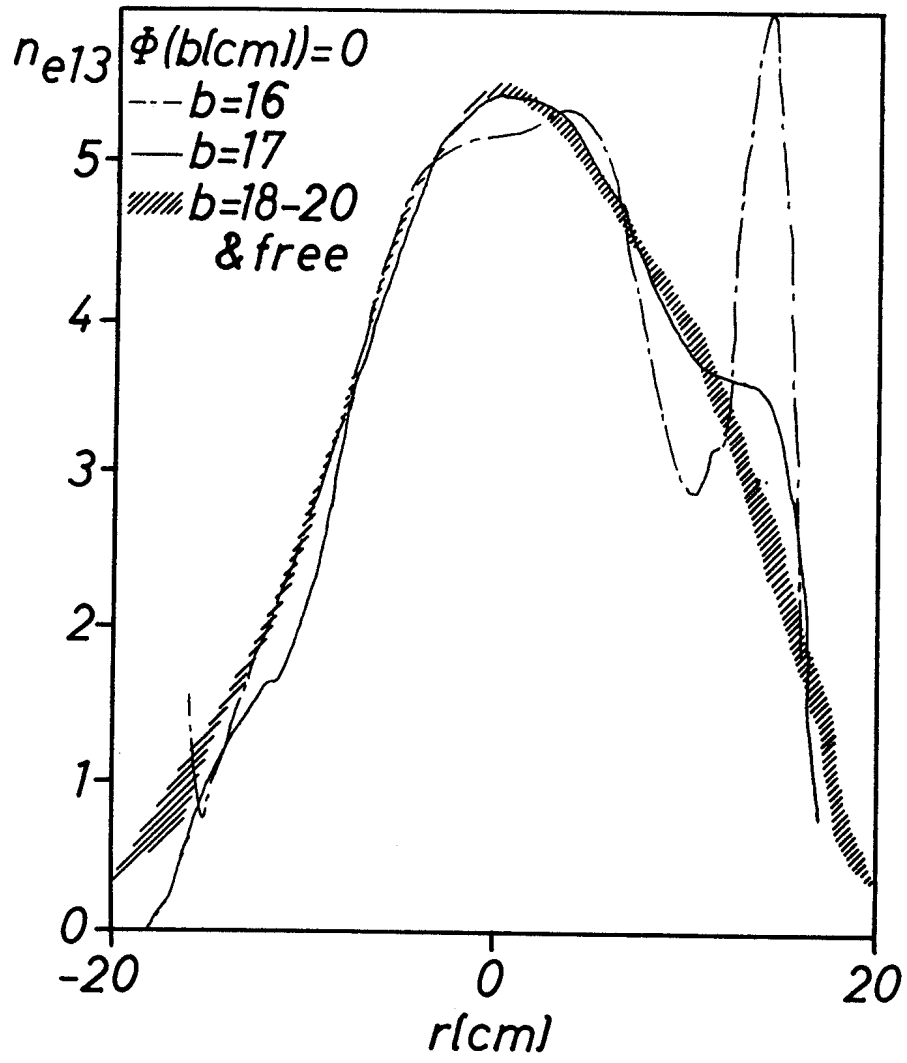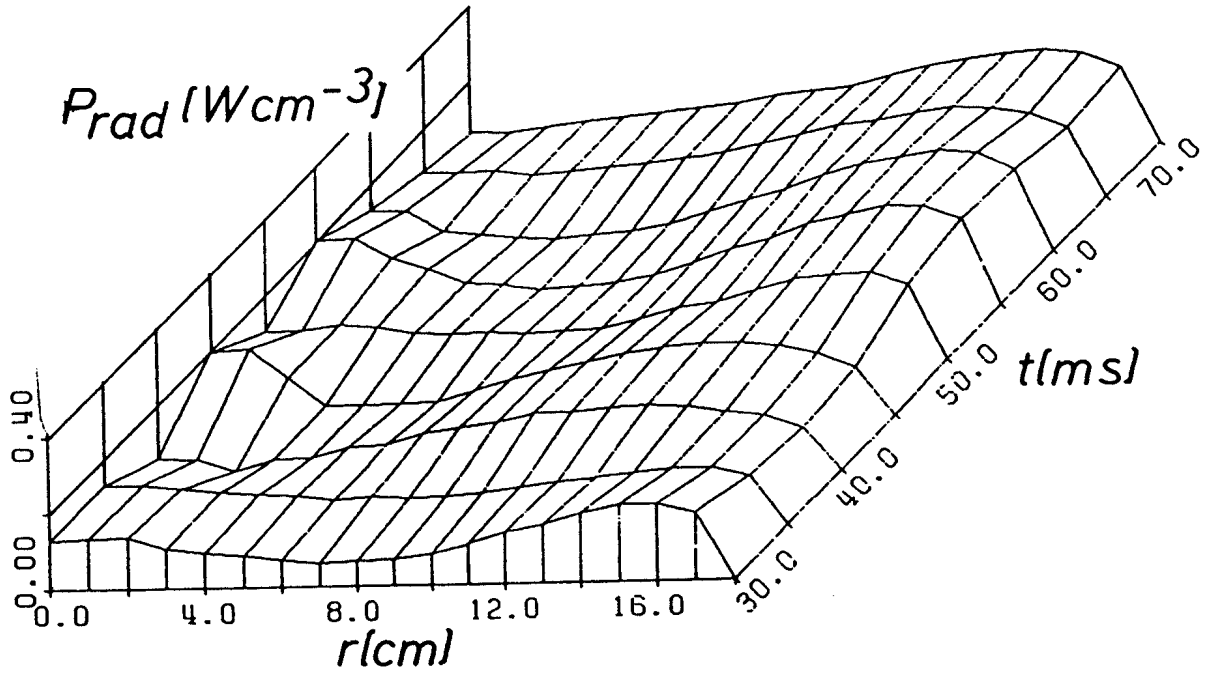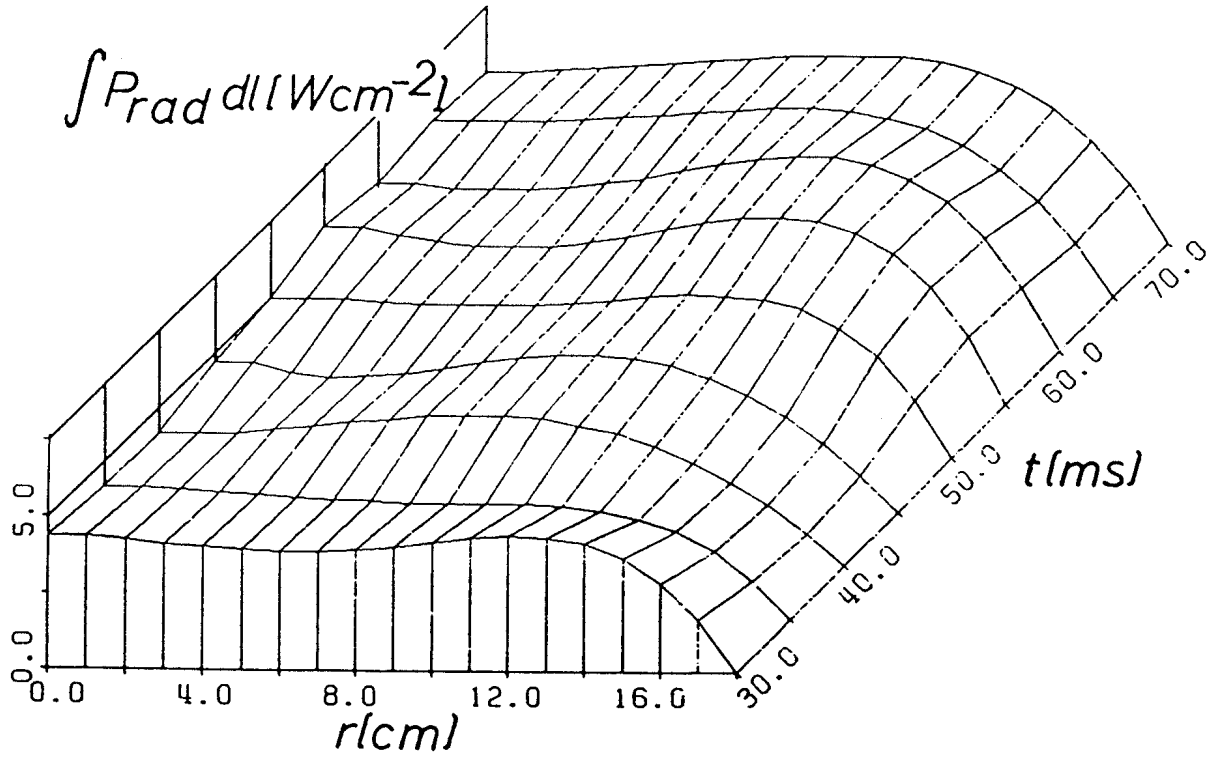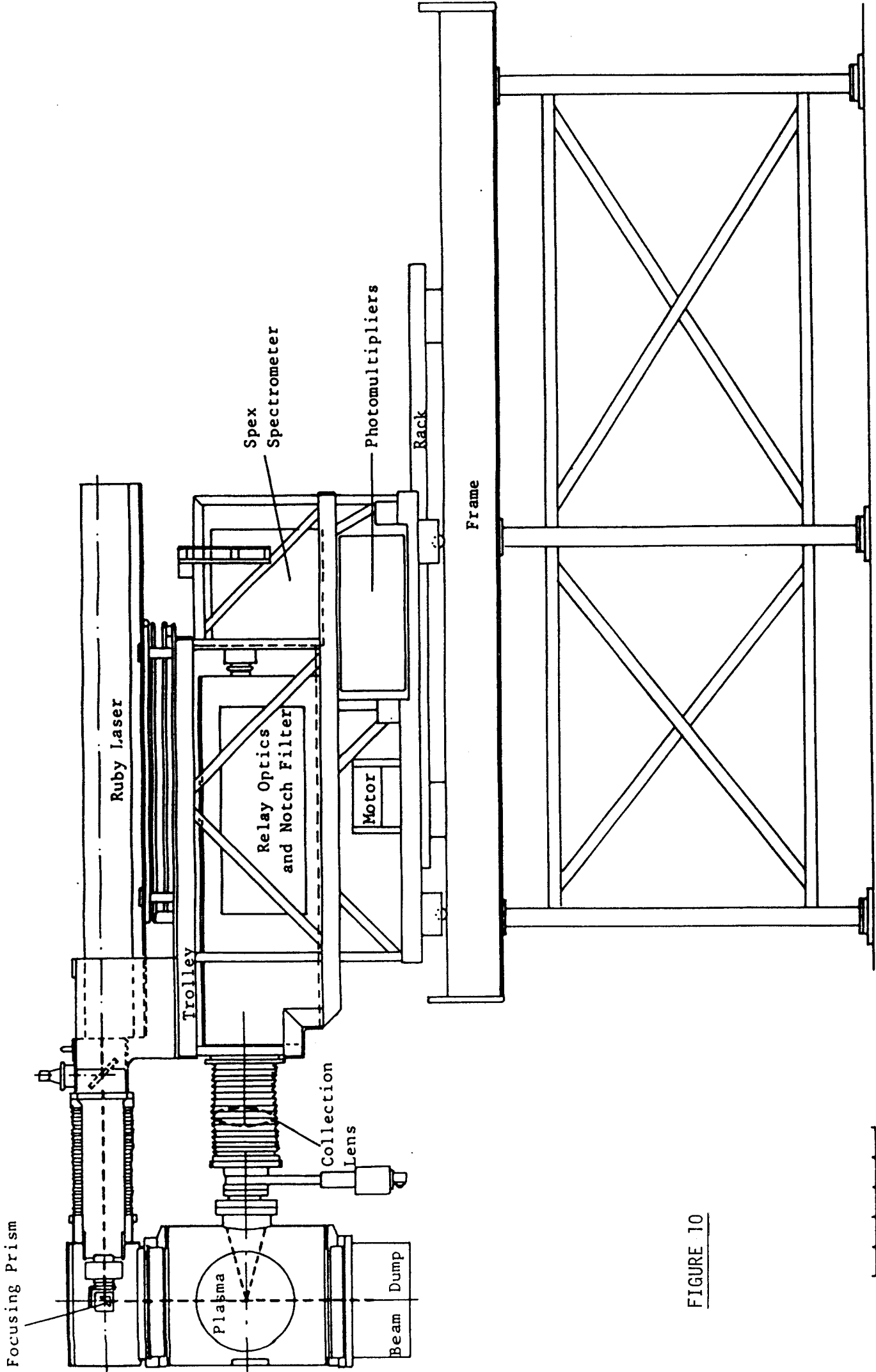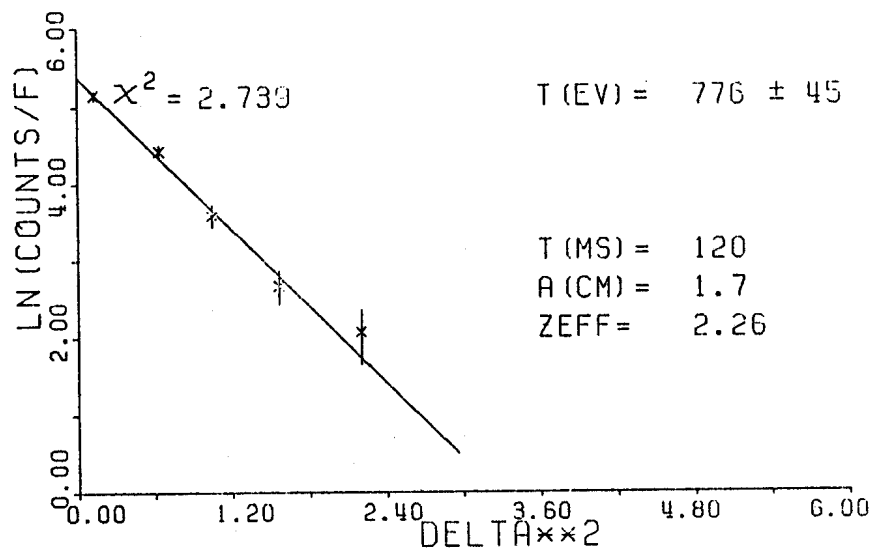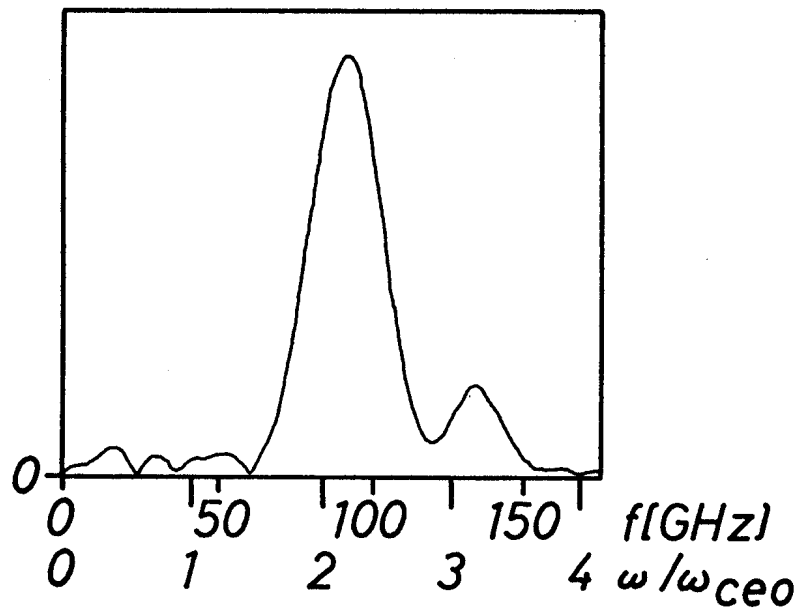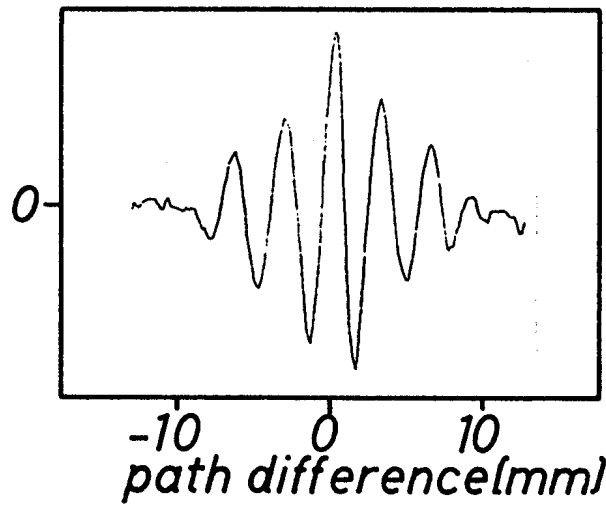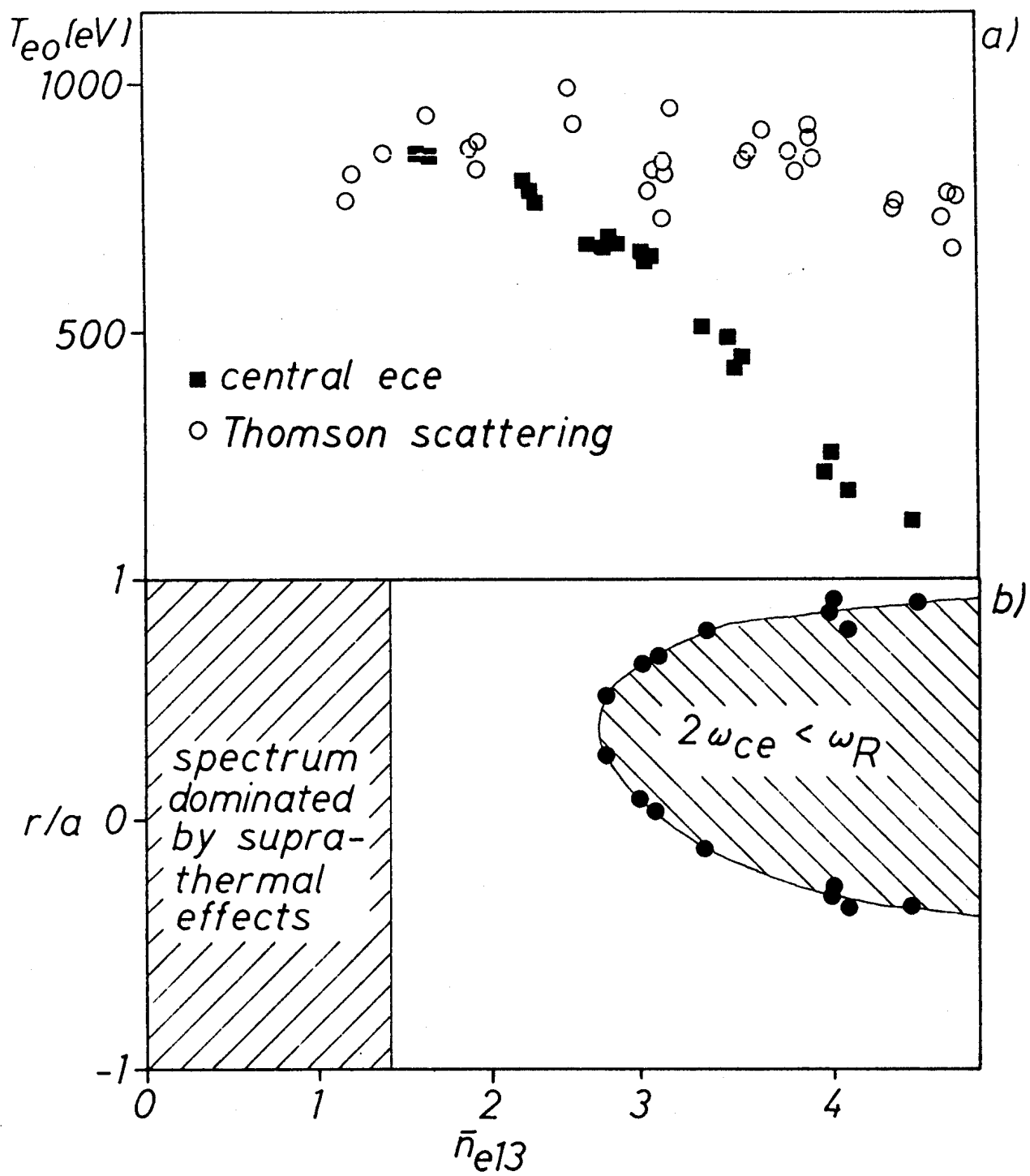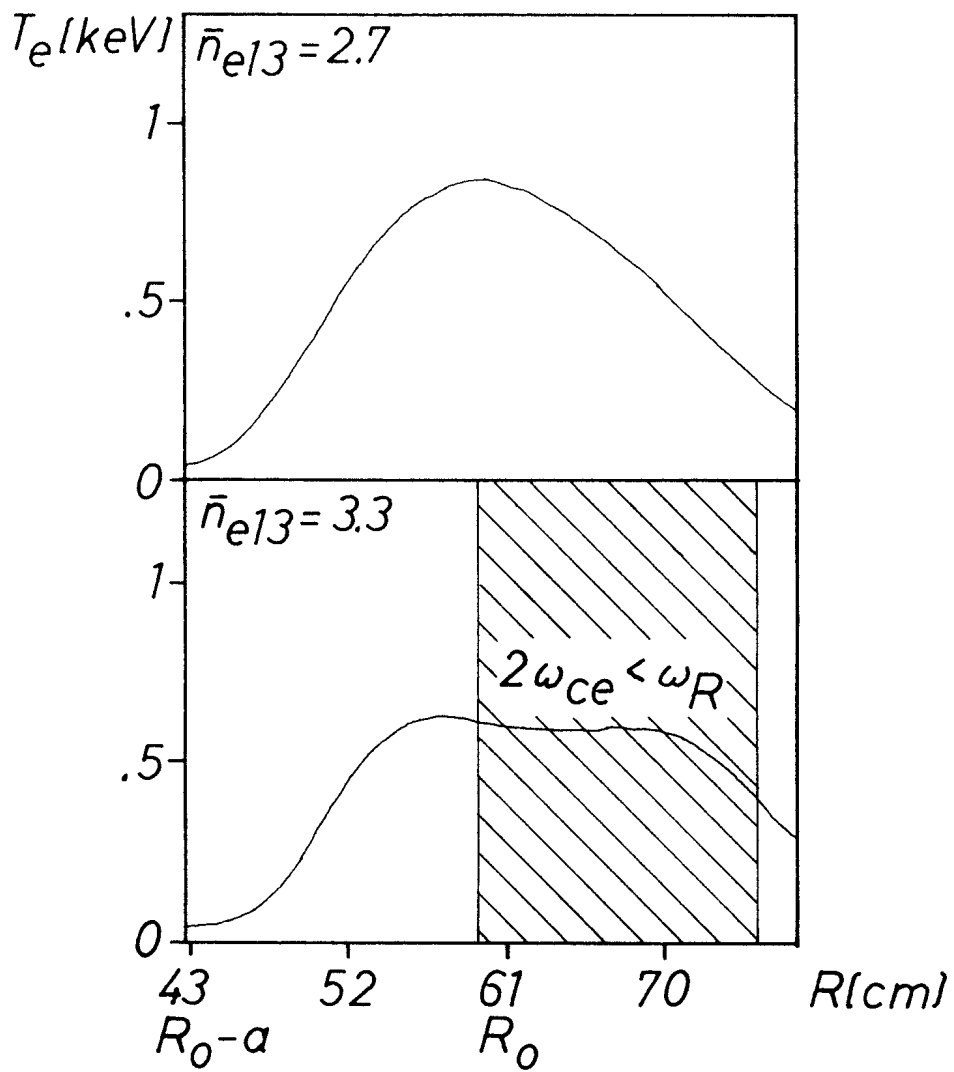
FIGURE 12

FIGURE 13

FIGURE 14
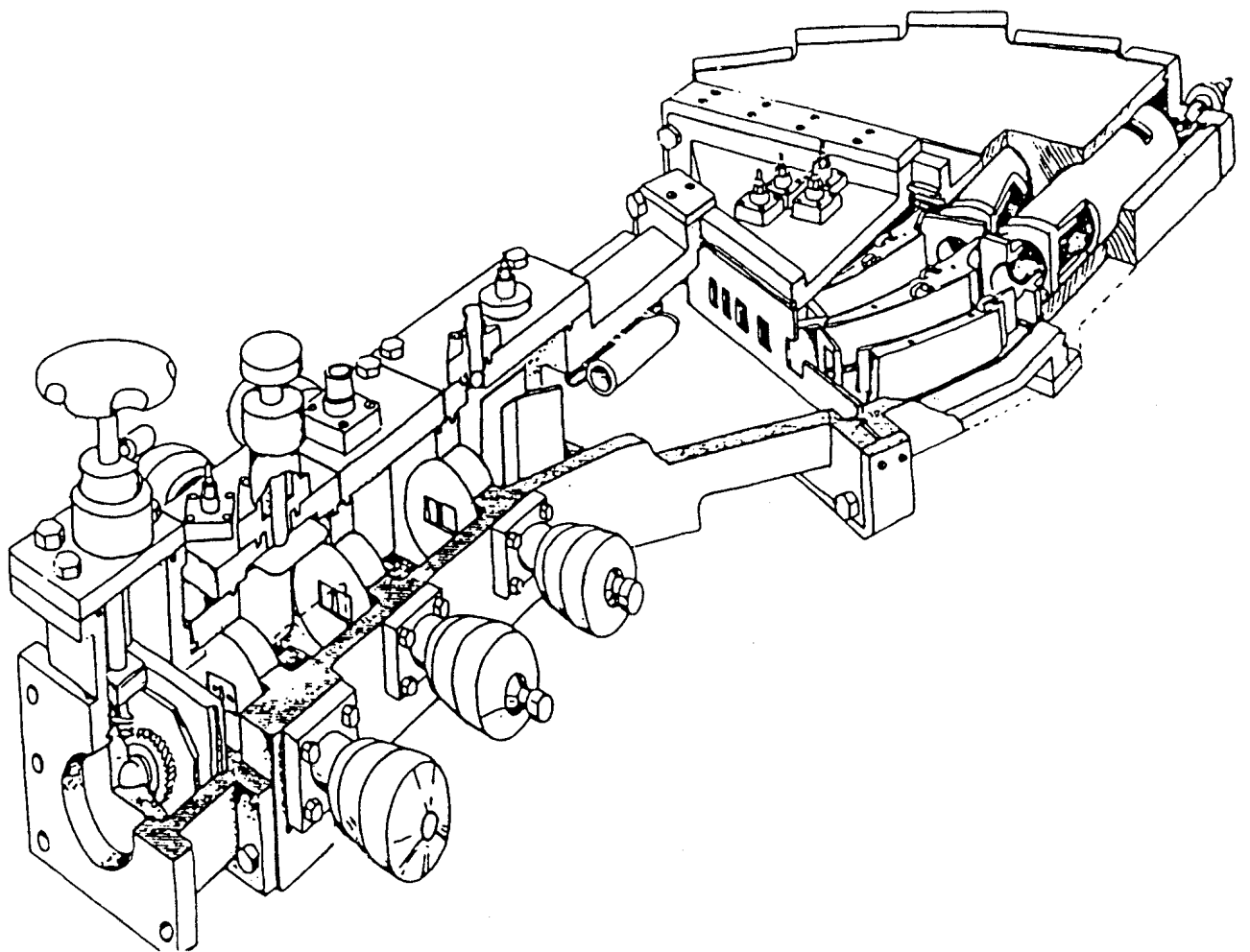
FIGURE 15
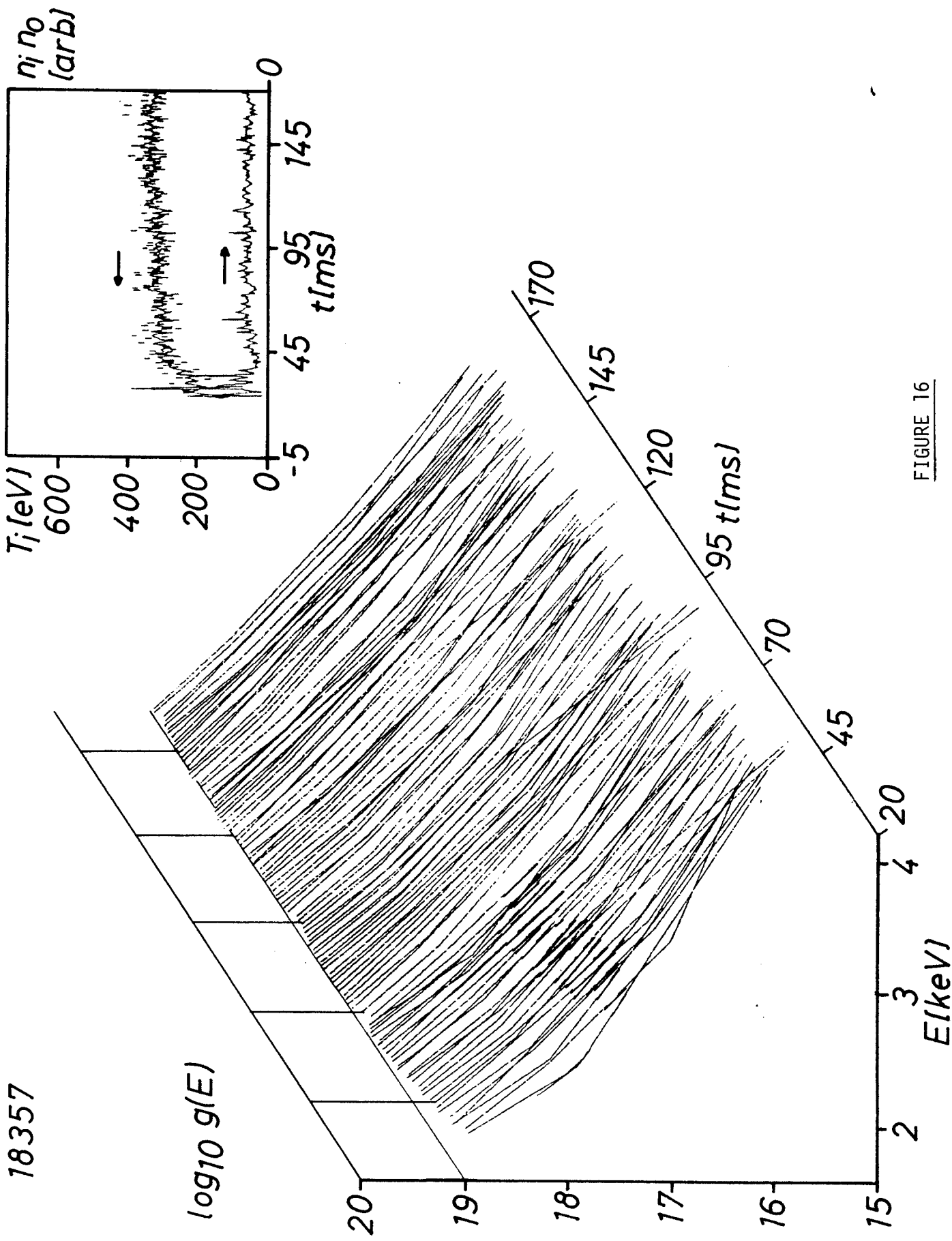
FIGURE 16
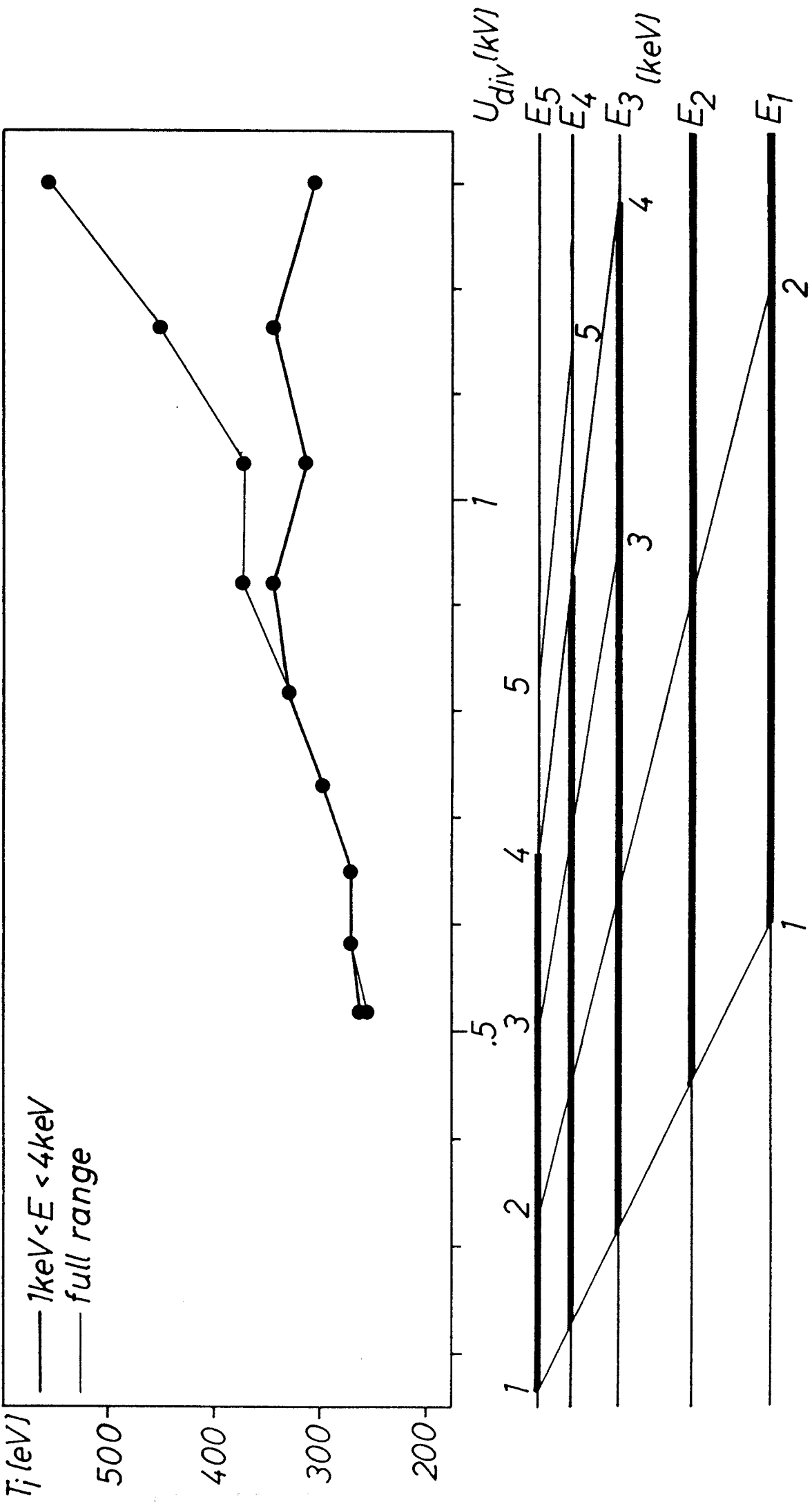
FIGURE 17
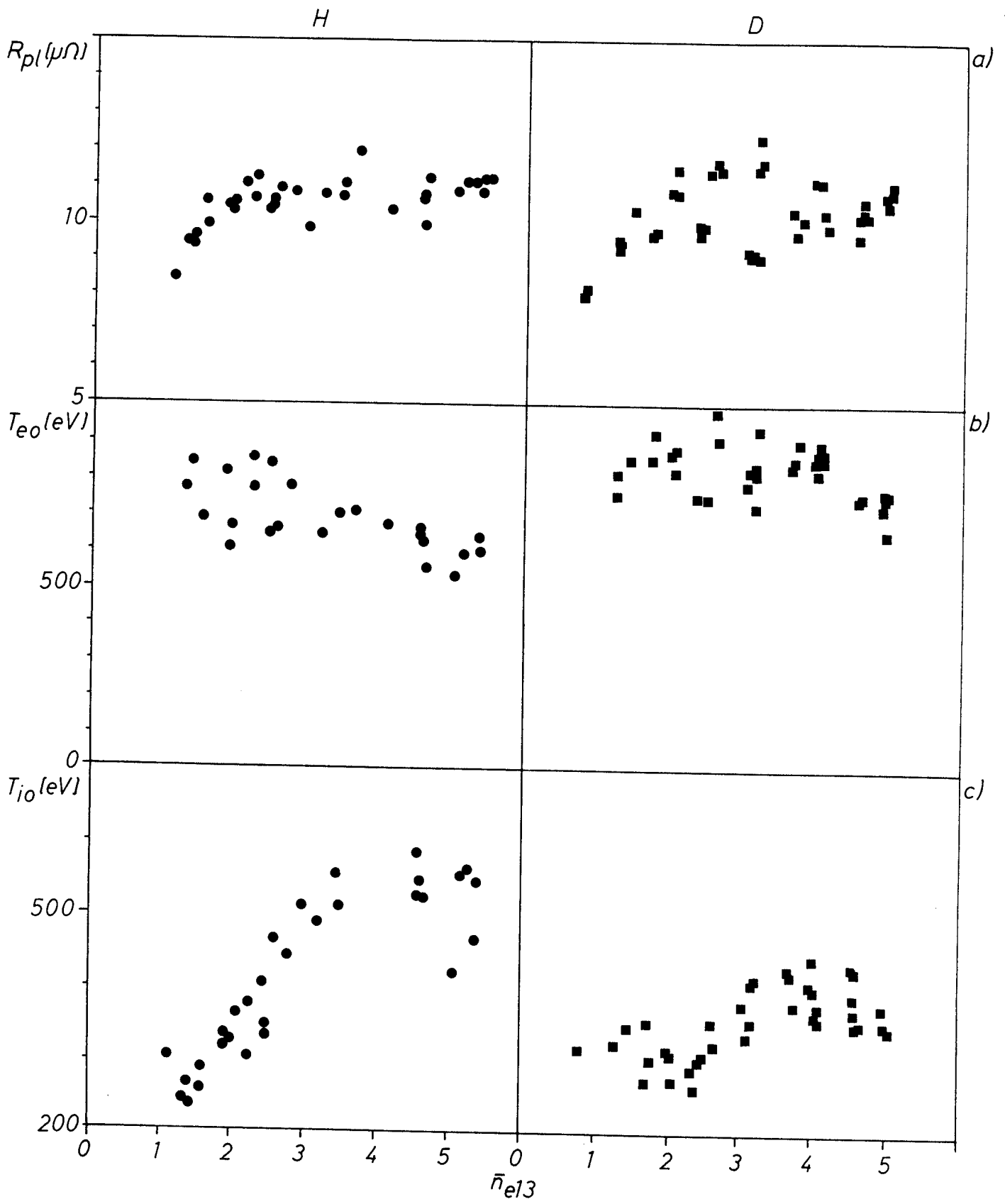
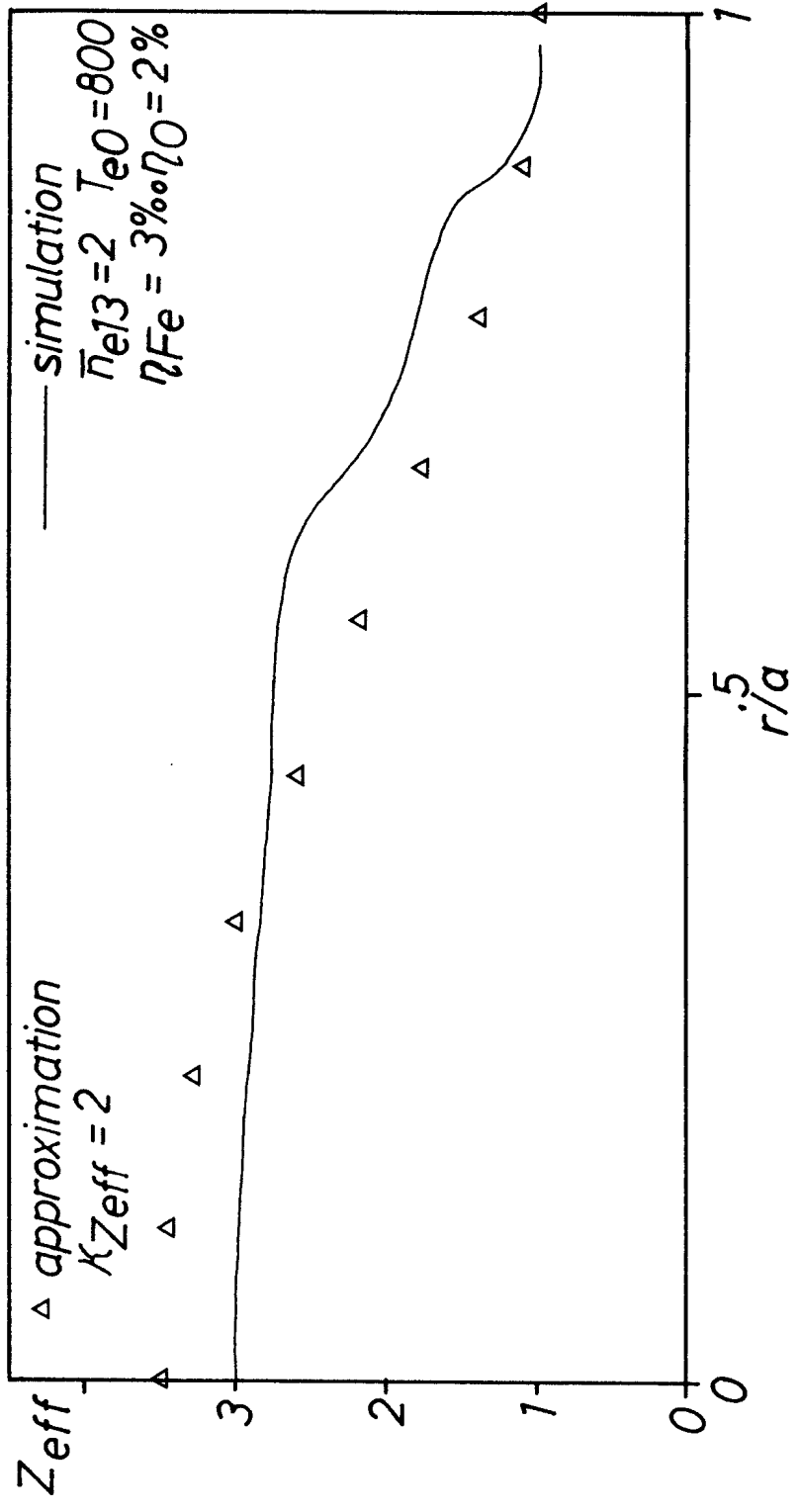FIGURE 18
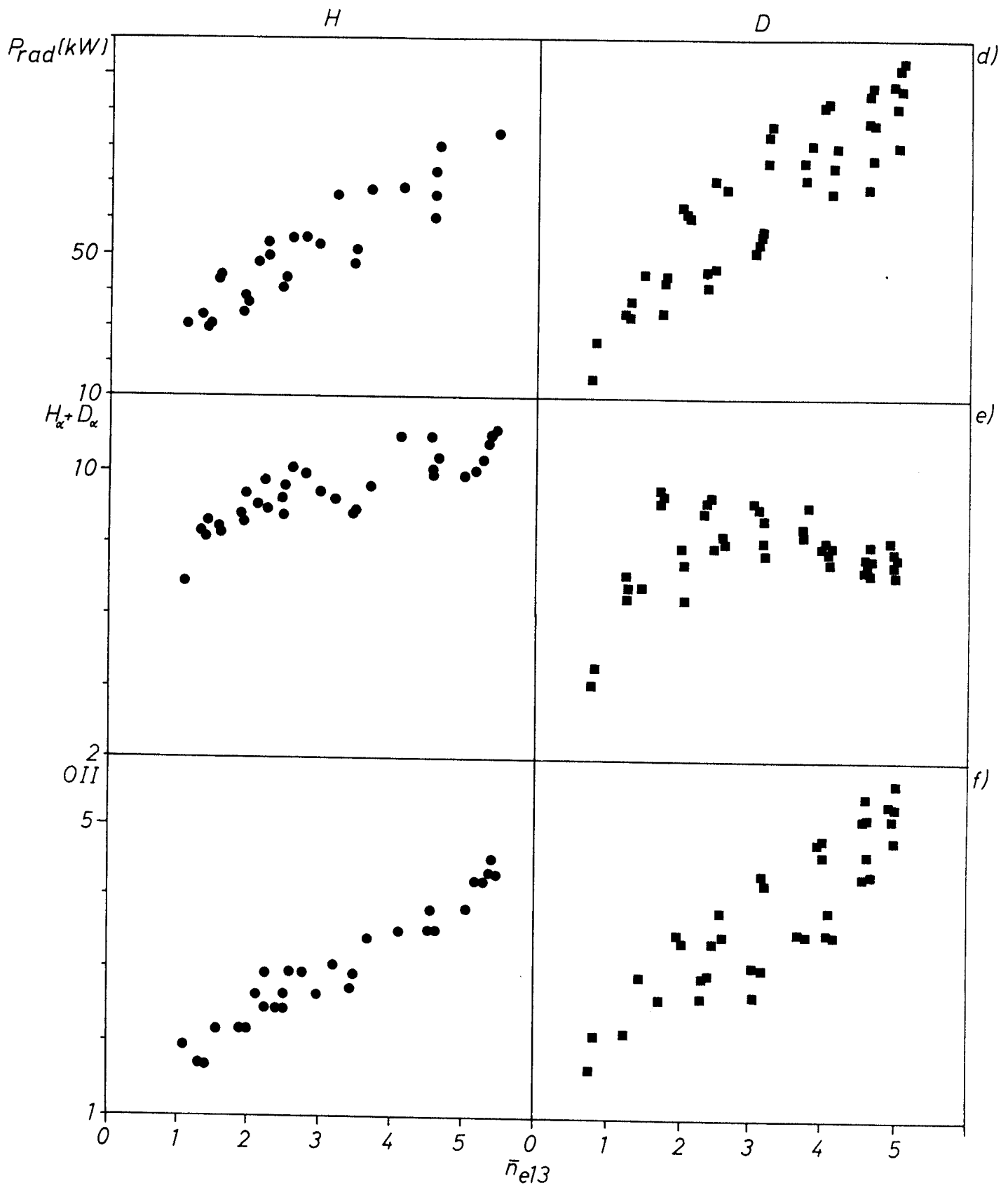
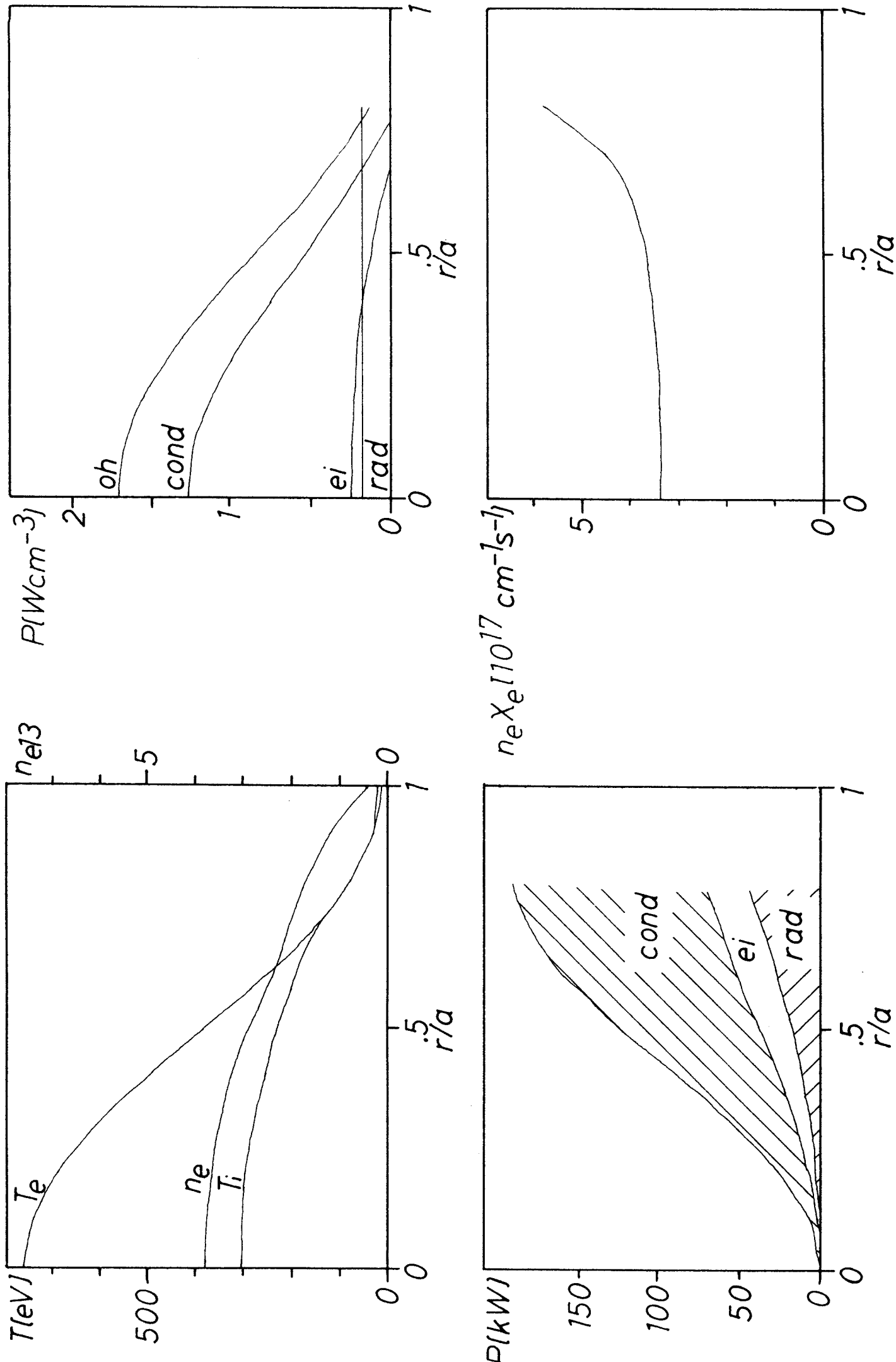FIGURE 18

FIGURE 18

FIGURE 18

FIGURE 19
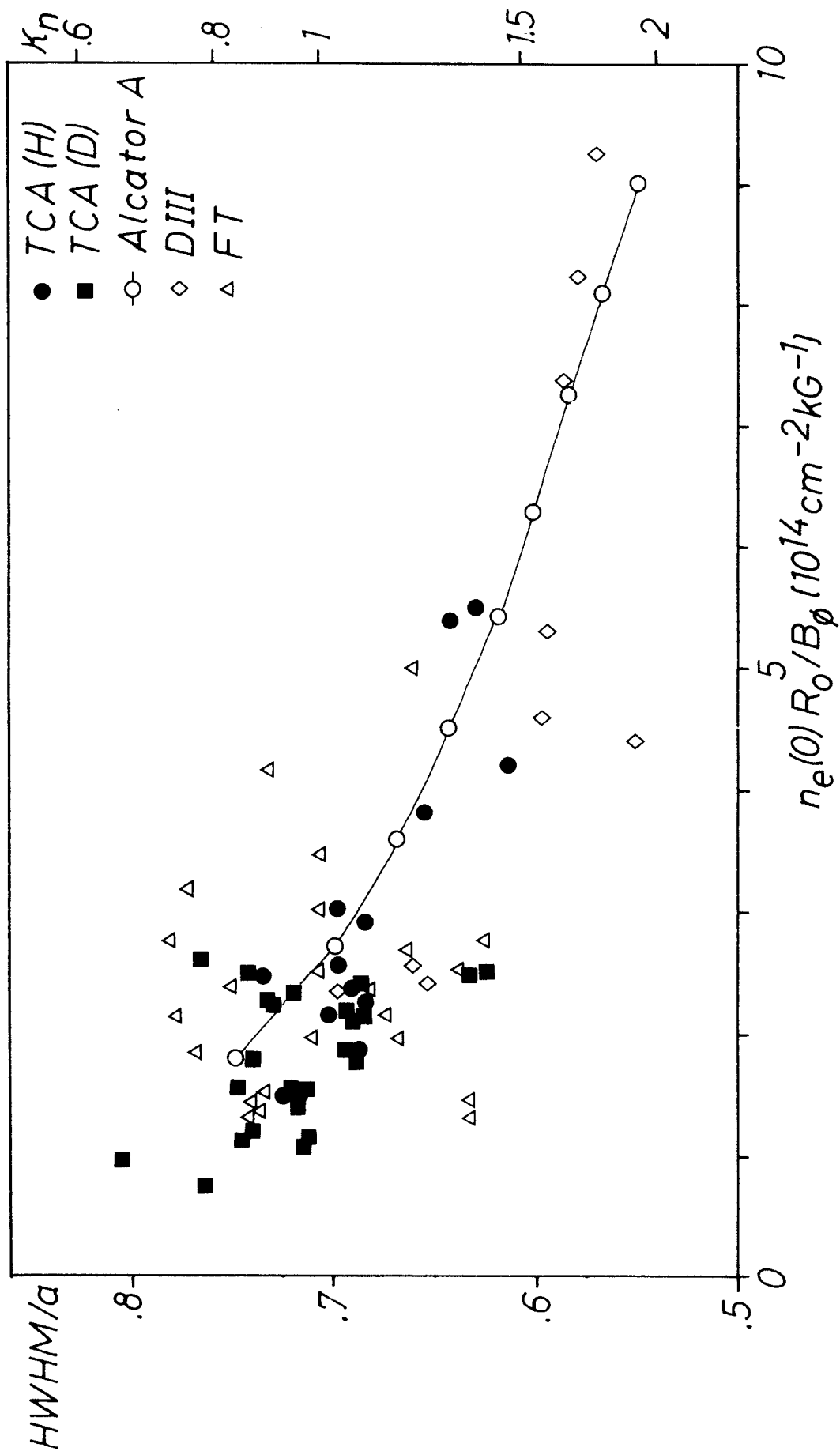
FIGURE 20
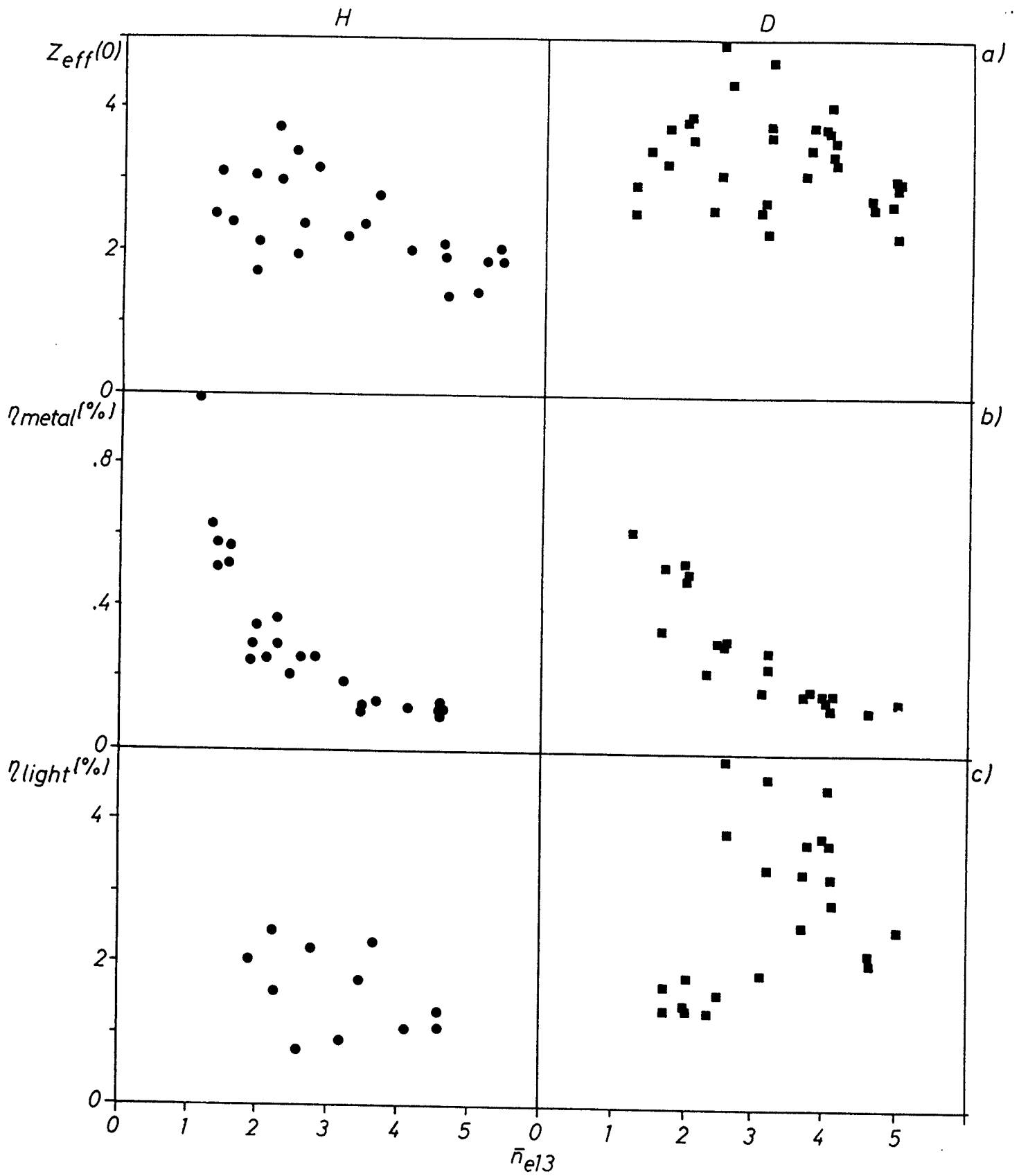
FIGURE 21
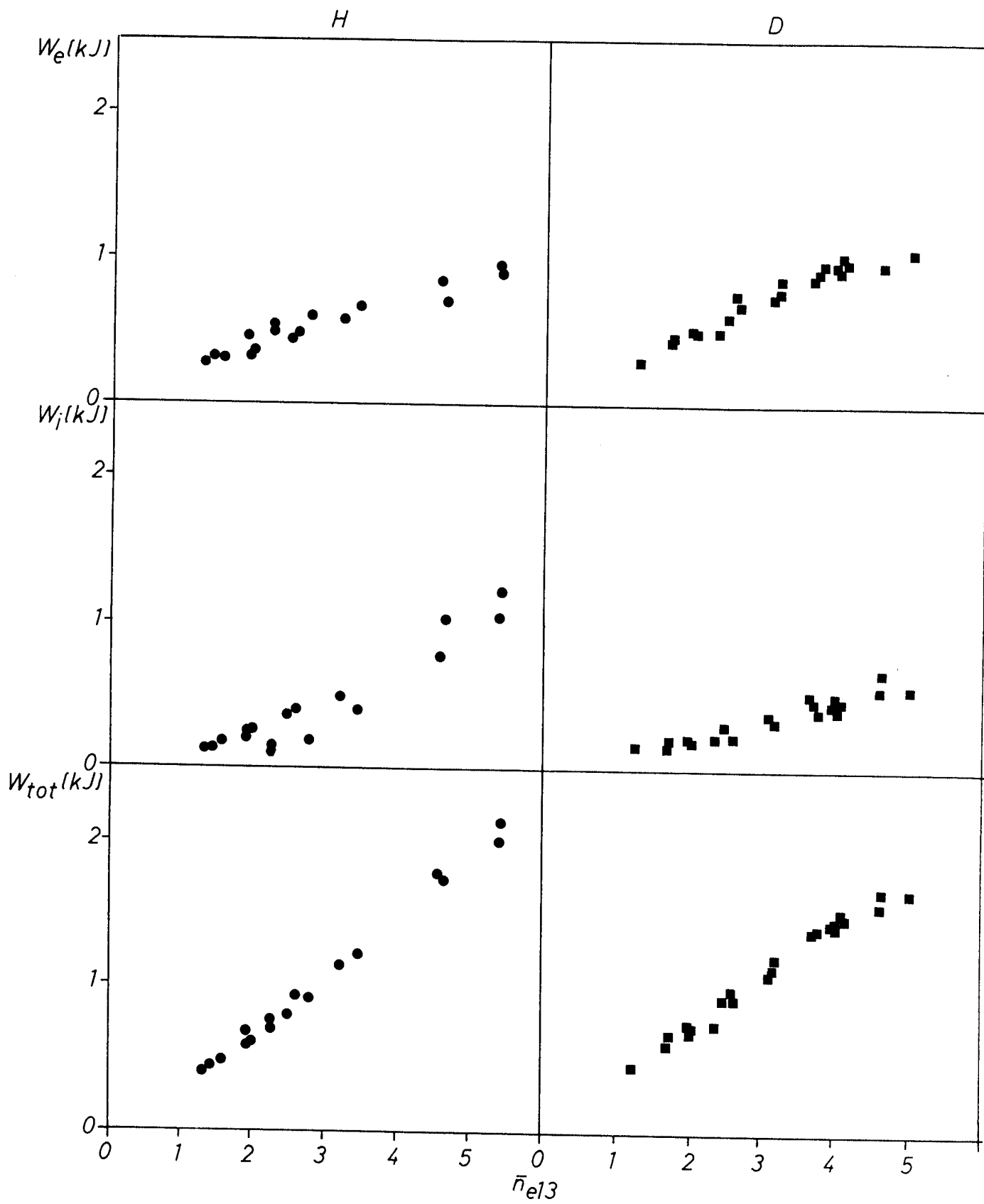
FIGURE 22
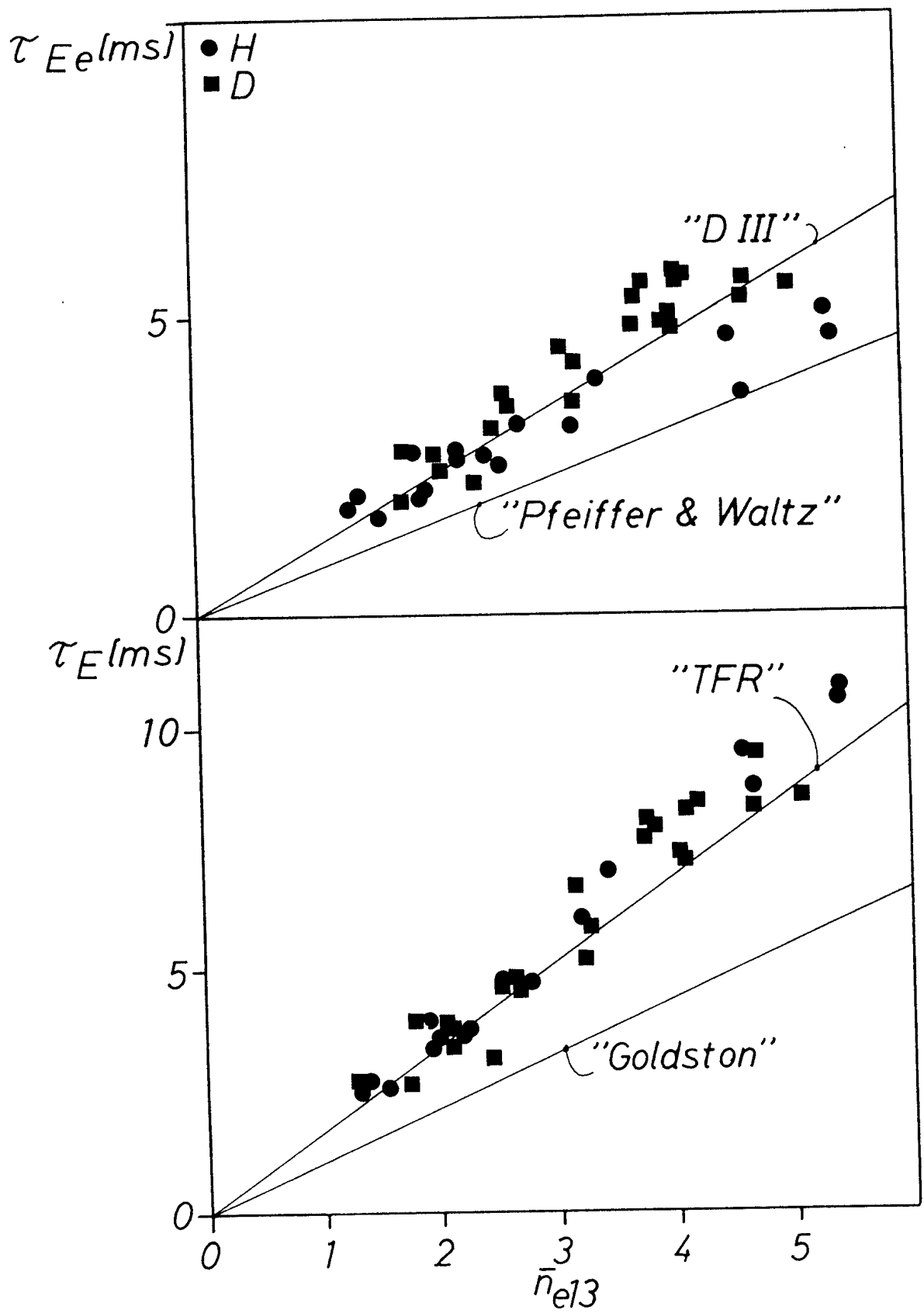
FIGURE 23

FIGURE 24

FIGURE 25

FIGURE 26